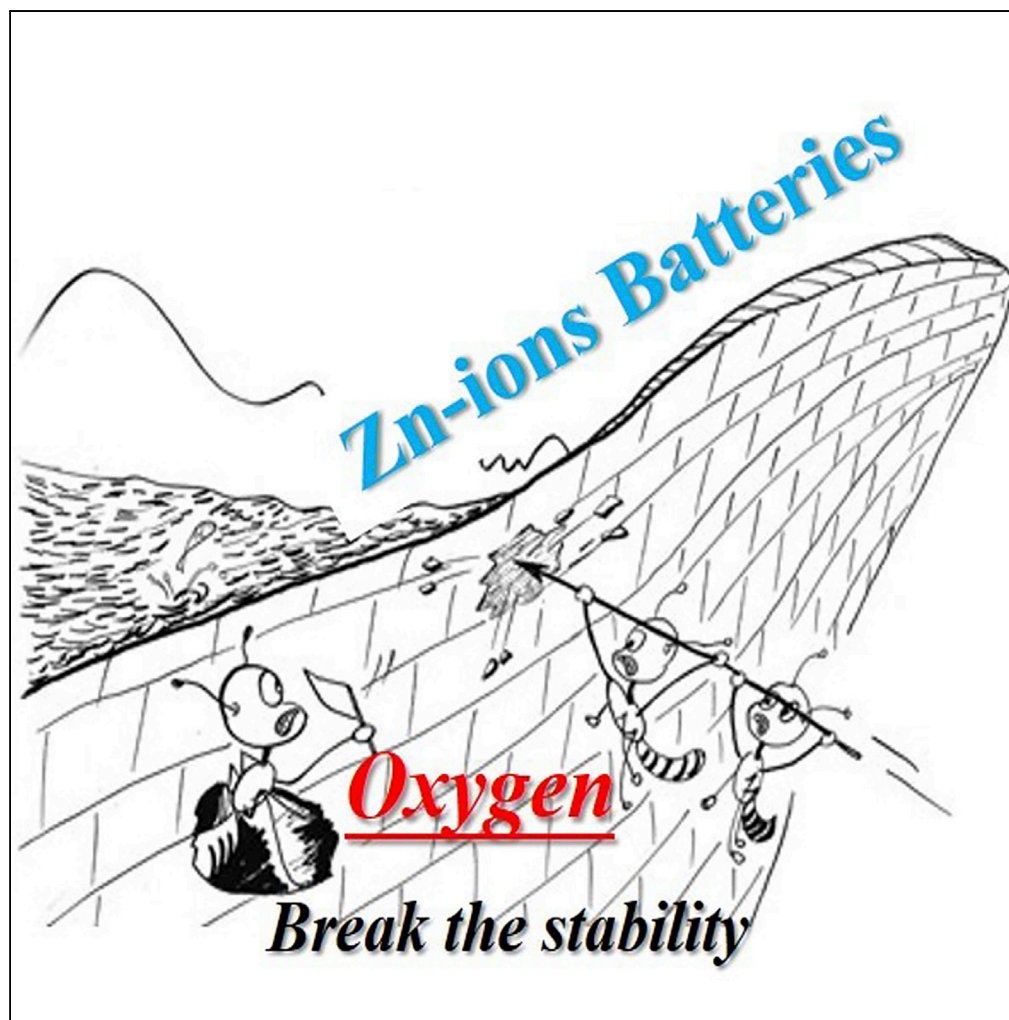


Article

Revealing the Impact of Oxygen Dissolved in Electrolytes on Aqueous Zinc-Ion Batteries



Lijun Su, Lingyang Liu, Bao Liu, Jianing Meng, Xingbin Yan

xbyan@licp.cas.cn

HIGHLIGHTS

Dissolved oxygen in electrolyte has significant impact on Zn anode and ZIBs

The dissolved oxygen caused the thermodynamically instability of Zn

Oxygen dissolved in electrolyte accelerates the corrosion on Zn

The ZIBs present better cycling stability after removing oxygen

Su et al., iScience 23, 100995
April 24, 2020 © 2020 The Author(s).
<https://doi.org/10.1016/j.isci.2020.100995>

Article

Revealing the Impact of Oxygen Dissolved in Electrolytes on Aqueous Zinc-Ion Batteries

Lijun Su,^{1,2} Lingyang Liu,^{1,2} Bao Liu,^{1,2} Jianing Meng,³ and Xingbin Yan^{1,2,4,5,*}**SUMMARY**

Aqueous zinc-ion batteries (ZIBs) are promising low-cost and high-safety energy storage devices. However, their capacity decay especially at the initial cyclic stage is a serious issue. Herein, we reveal that the dissolved oxygen in aqueous electrolyte has significant impact on the electrochemistry of Zn anode and ZIBs. After removing oxygen, the symmetrical set-up of Zn/Zn is capable of reversible plating/stripping with a 20-fold lifetime enhancement compared with that in oxygen enrichment condition. Taking aqueous Zn-MnO₂ battery as an example, although the presence of oxygen can contribute an extra capacity over 20% at the initial cycles due to the electrocatalytic activity of MnO₂ with oxygen, the corrosion of Zn anode can be eliminated in the oxygen-free circumstance and thus offering a better reversible energy storage system. The impact of the dissolved oxygen on the cycling stability also exists in other ZIBs using vanadium-based compounds, Birnessite and Prussian blue analog cathodes.

INTRODUCTION

Aqueous zinc-ion batteries (ZIBs) have gained more and more attention mainly due to their low cost as well as high safety (Parker et al., 2017; Zheng et al., 2019), and significant research progress has been achieved in designing aqueous ZIBs with Zn anode and various cathode materials (Trócoliand La Mantia, 2015; Sun et al., 2017; Pan et al., 2018; Wan et al., 2019). However, the reported ZIBs generally suffer poor cycling stability especially at the initial cycles. Taking the reported ZIBs using the most typical ZnSO₄ aqueous electrolytes as examples, whether the cathode material is vanadium oxides (Wan et al., 2018; Yang et al., 2018), manganese oxides (Mondoloni et al., 1992; Xu et al., 2012; Alfaruqi et al., 2015a, 2015b), Prussian blue analog materials (Zhang et al., 2015), and so on, all suffer significant capacity decay in the initial cycling stage (Table S1) (Fang et al., 2018; Song et al., 2018). Such decay was mainly explained because of the dissolution of cathode materials into the bulk electrolytes as well as the formation of Zn dendrite (Lee et al., 2014, 2016; Boeun et al., 2015; Mainar et al., 2018; Yi et al., 2018; Zhao et al., 2019a, 2019b).

On the one hand, it is well known that metal Zn is easily oxidized in the air (Mainar et al., 2018; Yi et al., 2018; Zhao et al., 2019a, 2019b). On the other hand, the dissolved oxygen is commonly more than 9 mg L⁻¹ in low-concentration aqueous electrolytes under ambient temperature and pressure, as high as the oxygen content in the air (Davis et al., 1967; Benson et al., 1979; Luo et al., 2010). Therefore, the oxygen dissolved in the aqueous electrolytes of ZIBs might oxidize the Zn anode, thereby impacting the performance of the devices. However, the study on the influence of the dissolved oxygen in electrolytes on the electrochemical properties of aqueous ZIBs is rare to date.

In this study, we demonstrate that the oxygen dissolved in aqueous ZnSO₄ electrolytes indeed cause significant impact on the reversibility and cycling stability of Zn anode and ZIBs. For Zn/Zn symmetrical cell, after removing the oxygen from the electrolyte, the cycling life can be increased about 20 times than that in the presence of oxygen. For aqueous Zn-MnO₂ battery, the presence of oxygen contributes an extra capacity over 20% to the cathode at the initial several cycles, but such capacity cannot be maintained in subsequent cycles. Instead, after removing the oxygen in advance, the decrease of capacity at the initial cycles is significantly suppressed, thus offering a more stable electrochemistry system. The impact of the dissolved oxygen on the cycling stability also exists in other aqueous ZIBs with cathodes of VO₂, V₂O₅, Na_{0.55}Mn₂O₄·1.5H₂O and K₂Zn₃[Fe(CN)₆]₂·(H₂O)₉.

¹Laboratory of Clean Energy Chemistry and Materials, Lanzhou Institute of Chemical Physics, Chinese Academy of Sciences, Lanzhou 730000, China

²Center of Materials Science and Optoelectronics Engineering, University of Chinese Academy of Sciences, Beijing 100049, China

³Cuiying Honors College, Lanzhou University, Lanzhou, 730000, China

⁴Dalian National Laboratory for Clean Energy, Chinese Academy of Sciences, Dalian 116023, China

⁵Lead Contact

*Correspondence: xbyan@licp.cas.cn

<https://doi.org/10.1016/j.isci.2020.100995>



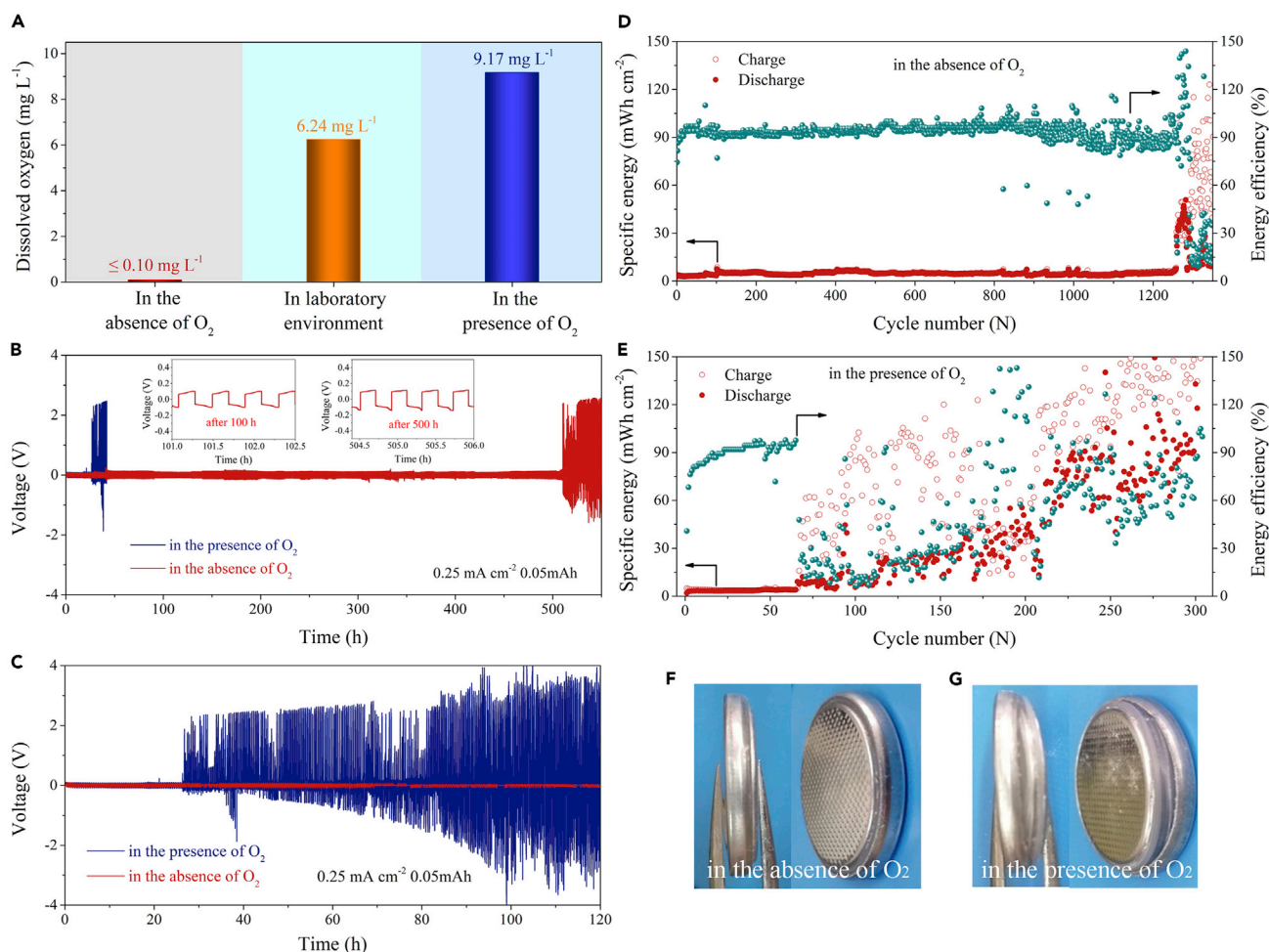


Figure 1. Electrochemical Characterization of Zn/Zn Cells

(A) The contents of O_2 in 2 M ZnSO_4 aqueous electrolyte at three different conditions: in the absence of O_2 , in laboratory environment, and in the presence of O_2 .

(B) Electrochemical stability and reversibility of the symmetrical Zn/Zn cell using 2 M ZnSO_4 aqueous electrolyte in the presence of O_2 and in the absence of O_2 , respectively, at a current density of 0.25 mA cm^{-2} and a charge/discharge cut-off capacity of 0.05 mAh. Insets are the galvanostatic charging-discharging curves of the Zn/Zn cell using the electrolyte in the absence of O_2 after 100-h and 500-h cycling.

(C) Electrochemical stability and reversibility of the symmetrical Zn/Zn cell in the presence of O_2 and in absence of O_2 with a cut-off cycling time of 120 h.

(D–G) The specific energy and energy efficiency of the symmetrical Zn/Zn cells (D) in the absence of O_2 and (E) in the presence of O_2 . Digital photographs of the Zn/Zn cells (F) in the absence of O_2 and (G) in presence of O_2 after the 120-h galvanostatic cycling.

RESULTS

Effect of Dissolved O_2 on Zn Anode

In order to study the impact of the dissolved O_2 in ZnSO_4 aqueous electrolyte on the reversibility and cycling stability of Zn anode and ZIB devices, we designed three electrolytes with different O_2 conditions: in the absence of O_2 (removing O_2 using high-purity nitrogen), in laboratory environment (containing naturally dissolved O_2), and in the presence of O_2 (inletting with high-purity oxygen to reach O_2 saturation). The corresponding dissolved O_2 contents are listed in Figure 1A. The dissolved O_2 in the 2 M ZnSO_4 aqueous electrolyte reached 6.24 mg L^{-1} in the open laboratory environment and in the presence of O_2 at room temperature, respectively. For comparison, the dissolved O_2 content after removing O_2 was reduced to less than 0.10 mg L^{-1} .

The electrochemical stability of Zn anode in the presence of O_2 and in absence of O_2 was evaluated by long-term galvanostatic cycling of symmetrical Zn/Zn coin cells (Chao et al., 2018). As shown in Figure 1B,

using the 2 M ZnSO₄ aqueous electrolyte in the presence of O₂, the Zn/Zn battery underwent a sudden and irreversible rise of the polarization voltage after cycling for 25 h at a current density of 0.25 mA cm⁻². When using a low current density, the Zn²⁺ ions undergo a deep deposition and exfoliation on the electrode. The generation of side reactions due to oxygen and changes in the stability of the battery are more easily detected under such a low current density in the Zn/Zn symmetrical cell (Pan et al., 2016; Chao et al., 2019; Yang et al., 2019; Zhao et al., 2019a, 2019b). In laboratory environment, the Zn/Zn cell also appeared distinct voltage polarization after 72 h (see Figure S1). As a contrast, as shown in Figure 1B, the Zn/Zn battery in the absence of O₂ displayed the best stability and reversibility for Zn plating/stripping. Specifically, after eliminating O₂, the cell exhibited a stable polarization voltage (~0.1 V) and a long-term galvanostatic cycling life of 510 h, representing a more than 20-fold improvement. The constant voltage curves after 100 and 500 h (insets of Figure 1B) also demonstrated the reversible Zn plating/stripping enabled in the absence of O₂.

Energy efficiency presents the energy loss of a ZIB battery during charging and discharging processes (Chiasserini and Rao, 2000; Simunic et al., 2001; Zhang et al., 2011; Hu et al., 2013), and it can reflect the degree of deposition and exfoliation of Zn ions at a certain overpotential, thereby reflecting the stability of the battery. As shown in Figure 1D, the high-and-stable energy efficiency (~90% after 1,260 cycles) indicated the long-term cycling stability for Zn plating/stripping in the absence of O₂. Comparatively speaking, the energy efficiency was unsatisfactory (less than 90%) after 65 and 180 cycles in the presence of O₂ (Figure 1E) and in open laboratory environment (Figure S2), respectively. Furthermore, as shown in Figure 1C, the voltage was hold in the stable state (less than 0.1 V) of the entire cycling within cut-off cycling time of 120 h in the absence of O₂. However, the voltage was significantly polarized after 26 h in the presence of O₂. In addition, after a 120-h galvanostatic cycling, the Zn/Zn battery was no obvious volume swell in the absence of O₂ (Figure 1F). For comparison, the battery showed obvious volume expansion in the presence of O₂ (Figure 1G). This indicated that the dissolved O₂ caused the thermodynamically instability of Zn and led to the hydrolysis of the electrolyte (Abdelall et al., 1992; Abdallah, 2003).

X-ray diffraction (XRD) characterization confirmed the corrosion of Zn after 120-h long-term galvanostatic cycling process. The pristine Zn showed no obvious zinc oxide, hydroxide, or zincate from its XRD pattern (JCPDS 87-0713, Figure S3), which is according with the result of scanning electron microscope (SEM) element mapping characterization (Figures S4A–S4C). For by-products on the surface of Zn plates, their peak positions were mainly concentrated within 5–35°. As shown in Figure 2A, there was a strong peak located at 8° for Zn plates both in the presence and absence of O₂, which corresponds to Zn₄(OH)₆SO₄·nH₂O (Pan et al., 2016; Jin et al., 2019). However, in the presence of O₂, there were more by-products (ZnO, Zn(OH)₂, and zincate) on the surface of Zn plates. As for ZnO, the distinct peaks located at 28.7, 31.1, and 33.7°. Moreover, the shoulder peak located 8.5° was related to the complexation of ZnO with SO₄²⁻ ions in the presence of O₂. Zn(OH)₂ on the Zn plate mainly concentrated at 16.1, 19.0, and 20.9° (Trócoli and La Mantia, 2015). Comparatively speaking, Zn plate in the absence of O₂ did not show obvious ZnO signal, and there were only two diffraction peaks of Zn₄(OH)₆SO₄·nH₂O at 8 and 24.3° as well as a characteristic peak of Zn(OH)₂ at 16.1°. This indicated that water and electrolyte ions can also cause slow corrosion on Zn plate in the absence of oxygen. Based on the above comparison, it can be verified that the Zn surface was severely corroded by O₂ in the presence of O₂ and formed a metal oxide/hydroxide layer, which caused electron insulation on the surface of Zn. Moreover, through the comparison of electrochemical impedance spectroscopies (EIS), it is shown that the presence of O₂ accelerated the corrosion of Zn during electrochemical cycling (Figure S5). The impedance increased by 100 orders of magnitude in the presence of O₂ (Figure 2C) than that in the absence of O₂ (Figure 2B). In addition, the corrosion on the surface of Zn in the absence of O₂ and in presence of O₂ after long-term cycling process was further confirmed by SEM (Figures S4D–S4I and S6) and atomic force microscope (AFM, Figure S7 and Table S2) characterizations.

The effect of O₂ on the Zn corrosion was further analyzed by linear polarization experiment in the 2 M ZnSO₄ electrolyte (Figure 2D). Compared with the Zn in the presence of O₂, the corrosion potential in the absence of O₂ increased from -1.004 to -0.973 V, and the potential offset was 31 mV. Most notably, the corrosion current in the absence of O₂ also reduced by 330 μA cm⁻². The more positive corrosion potential and the lower corrosion current indicated a less tendency of corrosion reaction as well as a lower corrosion rate (Abdelall et al., 1992; Stupnisek-Lisac et al., 1995; Abdallah, 2003). Thus, the result from the linear polarization experiment proved that the dissolved O₂ caused severe corrosion on the Zn plate.

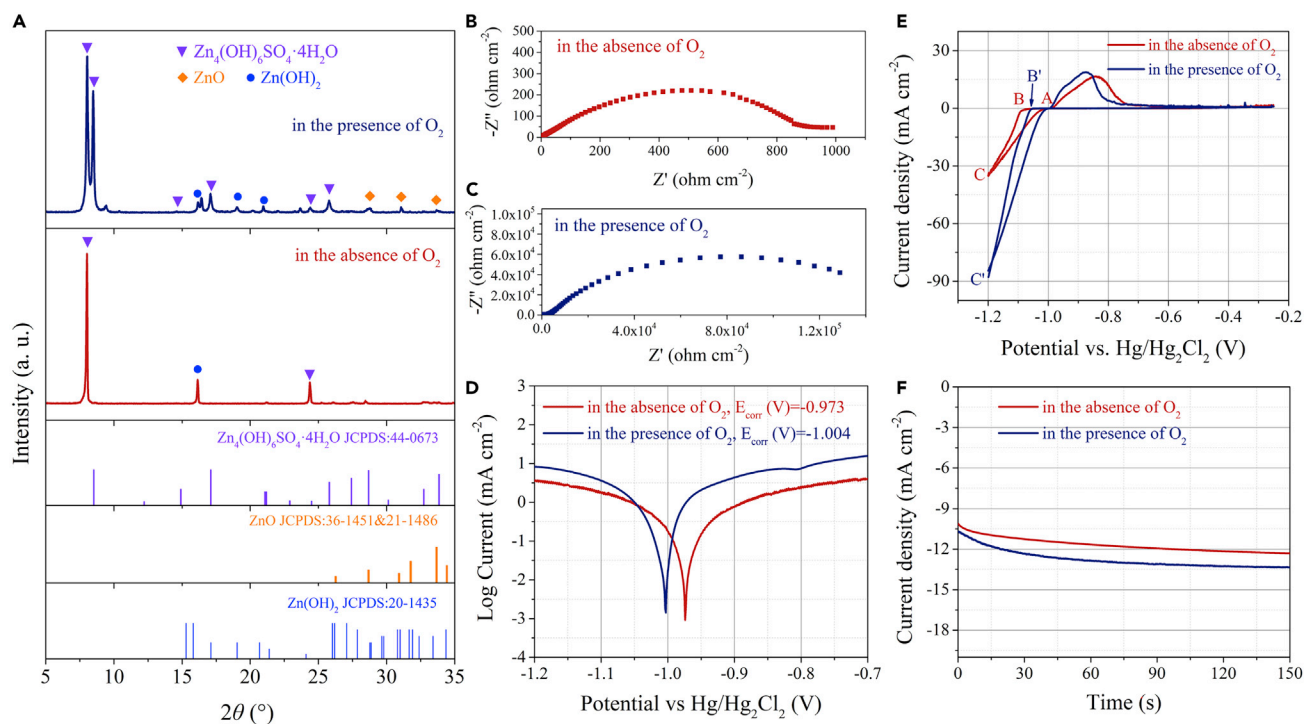


Figure 2. Effect of O_2 on Zn

(A–C) (A) X-ray diffraction (XRD) patterns of Zn after 120 h long-term galvanostatic cycling. Electrochemical impedance spectra (EIS) of symmetric Zn/Zn batteries in the absence of O_2 (B) and in presence of O_2 (C) after 120-h galvanostatic cycling.

(D) Linear polarization curves showing the corrosion on Zn in the absence of O_2 and in presence of O_2 .

(E) The nucleation cyclic voltammograms (CVs) in the absence of O_2 and in presence of O_2 .

(F) Chronoamperograms (CAs) of Zn at a -150 mV overpotential in the absence of O_2 and in presence of O_2 .

As shown in Figure 2E, cyclic voltammetry (CV) measurements were carried out in a three-electrode configuration in which Zn plate is the counter electrode, Ti is the working electrode, and saturated calomel electrode (SCE) is the reference electrode. When sweeping the potential toward more positive values, the nucleation process showed a crossover characteristic. The potential point of A was the crossover potential, and the point of B (or B') was the potential point of Zn^{2+} ions, which begins to be reduced. The potential offset between the crossover point (A) and the point (B or B') was known as the overpotential of nucleation (NOP). The value of NOP was the reference to judge the extent of electrode polarization (Mackinnon et al., 1987; MacKinnon et al., 1990; Tripathy et al., 1997; Zhang and Hua, 2009). Compared with the NOP in the presence of O_2 , the NOP elevated by 29 mV (56–85 mV) in the absence of O_2 . The higher overpotential indicated the adequate force for the growth and nucleation process (Pei et al., 2017).

Furthermore, the application of a -150 mV overpotential to the chronoamperometry (CA) test was conducted, and the corresponding result is shown in Figure 2F. The ever-increasing current density indicated the rampant diffusion and rough deposition process (Diggle and Damjanovic, 1972; Trejo et al., 2001; Wang et al., 2001, 2006; Lan et al., 2007). Zn^{2+} ions more likely diffuse along the energetically favorable sites for charge transfer on the surface (Ballesteros et al., 2007; Zhao et al., 2019a, 2019b). Moreover, Zn^{2+} ions tend to grow into dendrites for the sake of the minimum surface energy and the exposed area (Ballesteros et al., 2007). In this study, in the absence of O_2 , the initial Zn nucleation and 2D diffusion processes occurred within 20 s from the CA plots. Then, at a current density of 12 mA cm^{-2} , the 3D diffusion processes become constant and stable, which indicated the appeared of constrained 2D surface diffusion of the locally Zn^0 . This was because Zn^{2+} ions were tended to be uniformly deposited on the 2D plane in an O_2 -free environment. In the presence of O_2 , during the initial nucleation process, because Zn^{2+} ions were tended to grow toward the lowest surface energy, the deposition was heterogeneous and unstable.

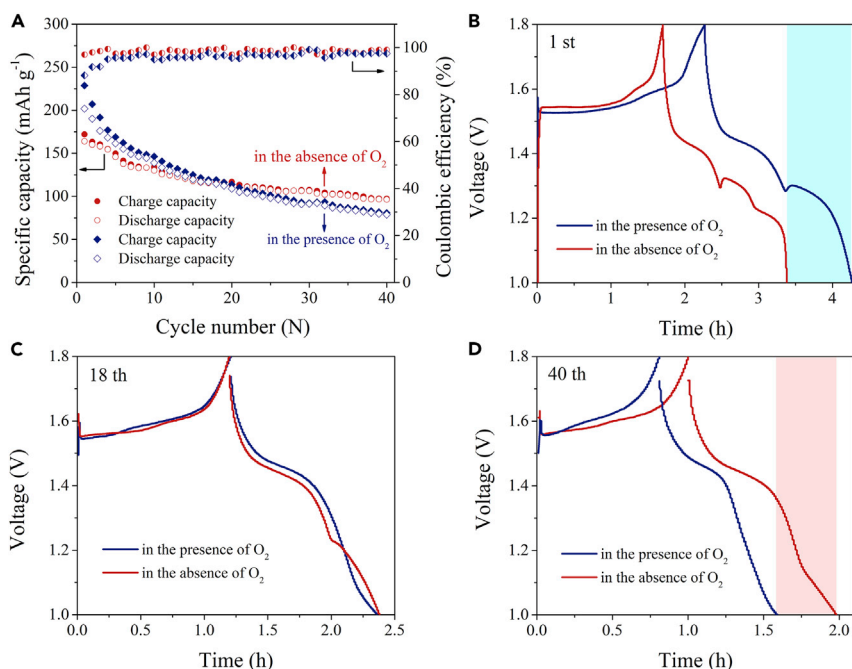


Figure 3. Electrochemical Characterization of Aqueous Zn-MnO₂ Batteries

(A) Cycling stability at 0.1 A g⁻¹ in the presence of O₂ and in absence of O₂.

(B–D) Galvanostatic charge and discharge (GCD) curves at different cycles: (B) the first cycle, (C) the 18th cycle, and (D) the 40th cycle.

Through the above analyses, we conclude that the O₂ dissolved in ZnSO₄ aqueous electrolyte accelerates the corrosion on the Zn surface and generates by-products such as zinc oxide, zinc hydroxide, and zincate. The by-products with insulation property irreversibly increase the electrochemical impedance of Zn, thereby resulting in the instability of symmetric Zn/Zn battery.

DISCUSSION

Effect of Dissolved O₂ on Zn-MnO₂ Battery

In order to study the impact of the dissolved O₂ on ZIB devices, we constructed Zn-MnO₂ batteries using α -MnO₂ nanofibers as cathode material that were synthesized by hydrothermal method. Figures S8 and S9 show the microstructure of α -MnO₂ nanofibers. Firstly, an aqueous Zn-MnO₂ battery was assembled using 2 M ZnSO₄ electrolyte in the open laboratory environment (the content of dissolved O₂ was 6.24 mg L⁻¹). As shown in Figure S10A, although a high reversible capacity was delivered in the first cycle (173 mAh g⁻¹ at a current density of 0.308 A g⁻¹), a rapid capacity deterioration was observed upon cycling. The specific capacity was decreased from 173 to 21 mAh g⁻¹ after 600 cycles, and the capacity retention rate was only 12.1%. Especially in the initial tens of cycles, the capacity showed cliff-type decay. This capacity fading was explained because of the dissolution of Mn²⁺ from Mn³⁺ disproportionation into the electrolyte and the formation of Zn dendrite during cycling (Lee et al., 2014; Alfuruqi et al., 2015a, 2015b; Boeun et al., 2015; Mathew et al., 2015).

Following, aqueous Zn-MnO₂ batteries were assembled using 2 M ZnSO₄ electrolytes in the presence of O₂ and in absence of O₂, respectively, and the comparison of their cycling performance is shown in Figure 3A. The initial capacity of the aqueous Zn-MnO₂ battery in the absence of O₂ was less than that in the presence of O₂ (164 mAh g⁻¹ compared with 202 mAh g⁻¹ at 0.1 A g⁻¹). Here, the α -MnO₂ used in Zn-MnO₂ batteries has been widely reported in some high-level literatures, and all the reported works showed that the depth of charge/discharge was approximate with that employed in our work (Pan et al., 2016; Chen et al., 2017; Fang et al., 2018; Song et al., 2018; Zheng et al., 2019). We compared the cycling stability of aqueous Zn/MnO₂ batteries using 2 M ZnSO₄ electrolytes in the presence of O₂ and in absence of O₂ at 0.1 A g⁻¹ without adding conductive graphite of cathode material (Figure S11). A high reversible capacity was delivered in the first cycle in the presence of O₂. Thus, the extra charge capacity was not due to the

oxidation of conductive graphite. Nevertheless, the battery showed a better cycling stability in the absence of O_2 (60% of capacity retention) than that in the presence of O_2 (38% of capacity retention) after 40 cycles. Galvanostatic charge and discharge (GCD) curves also showed the aqueous Zn-MnO₂ battery in the presence of O_2 exhibited a higher capacity within the initial cycles than that in the absence of O_2 (Figure 3B), and the former had an obvious discharge platform at the third stage. But after the rapid capacity attenuation, the capacity in the presence of O_2 was approximate with that in the absence of O_2 at 18 cycles (Figure 3C). After 40 cycles, its capacity was obviously lower than that in the absence of O_2 (Figure 3D), and the third discharge platform disappeared as well. Such reaction process may correspond to the $ZnSO_4[Zn(OH)_2]_3 \cdot xH_2O$ discharge product. The presence of $ZnSO_4[Zn(OH)_2]_3 \cdot xH_2O$ indicated the H^+ conversion reaction with MnO₂ cathode to form MnOOH during the third discharge platform. Meanwhile, the OH^- reacted with the Zn^{2+} ions, which dissolved from Zn anode and $ZnSO_4$ aqueous electrolyte to form the accompanied discharge compound of $ZnSO_4[Zn(OH)_2]_3 \cdot xH_2O$ on MnO₂ electrode along with the redox reaction of $MnO_2 + H^+ + e^- \leftrightarrow MnOOH$ (Pan et al., 2016; Jin et al., 2019). In addition, the Zn anodes of two batteries were subjected to SEM characterization after cycling (Figure S12). It was observed that the Zn anode was severely corroded in the cycled battery using the electrolyte with O_2 . Similarly, when widening the voltage window to 1–1.9 V, the corresponding Zn-MnO₂ battery exhibited a faster capacity attenuation in the O_2 -rich environment (Figure S10B). The results proved that the existence of dissolved O_2 indeed resulted in the corrosion of Zn anode and thus aggravated the capacity decay of the Zn-MnO₂ battery. We conclude other might reasons that caused the rapid capacity fading of Zn-ion batteries. The insertion of proton and hydrogen evolution during recharge is the reason for the rapid capacity fading—the proton produced from the $ZnSO_4$ electrolyte and the hydrolysis of water ($H_2O \leftrightarrow H^+ + OH^-$). The growth of notorious Zn dendrites as well as their poor electrochemical and thermodynamic characteristics have been the bottleneck that restrict Zn-ion batteries for long cycling stability. More importantly, because of incessant complex Faraday and non-Faraday side reactions in ZIBs, the Zn^{2+} -insulating by-products, such as Zn oxides, hydroxides, and zincates, can passivate the fresh Zn. In addition, the dissolution of electrode materials into the bulk electrolyte is another reason for the capacity fading in aqueous Zn-ion batteries (Pan et al., 2016; Fang et al., 2018; Song et al., 2018).

O_2 Dissolved in Electrolyte on the Energy Storage Electrochemistry

For a deeper understanding of the effect of O_2 dissolved in electrolyte on the energy storage electrochemistry of Zn-MnO₂ battery, we investigated the influence of O_2 on the electrochemical properties of α -MnO₂ cathode, including the GCD, linear sweep voltammetry (LSV), and b values. In ambient of O_2 , the initial charge voltage profile exhibited a flat plateau at 1.52 V, and then a voltage plateau from 1.65 to 1.8 V was observed (Figure 4A). It was evidently different from that occurred in the absence of O_2 (Figure 4B), where the charge voltage profile showed a flat plateau at 1.54 V, and then the slope of voltage curve ascended without obvious plateau from 1.65 to 1.8 V. The average operating voltages of α -MnO₂ were 1.44 V (in the presence of O_2) and 1.41 V (in the absence of O_2), and the nontrivial overpotentials were 204.2 mV (in the presence of O_2) and 227 mV (in the absence of O_2) at the first cycle. Moreover, the battery in the presence of O_2 contributed more capacity (over 20%) than that in absence of O_2 at the first cycle.

As shown in Figure 4C, α -MnO₂ electrode exhibited a smaller overpotential (58 mV) at 5 mA cm^{-2} in the presence of O_2 than that in the absence of O_2 . LSV characterization indicated that, although the oxygen evolution reaction (OER) catalytic activity of the α -MnO₂ was unsatisfactory when compared with some typically reported OER catalysts (Ma et al., 2018; Pendashteh et al., 2019; Shinde et al., 2019), the hydrolysis was easier in the O_2 -rich environment. Subsequently, the corresponding Tafel slopes were analyzed to show the OER catalytic kinetics (Ma et al., 2018). As shown in Figure 4D, α -MnO₂ exhibited a Tafel slope of 226 mV dec^{-1} in the presence of O_2 , lower than that in the absence of O_2 (324 mV dec^{-1}), which suggested the improved OER kinetics performance of the α -MnO₂ electrode in the presence of O_2 . Moreover, the b value of the Zn-MnO₂ battery in the presence O_2 (Figure 4E) demonstrated a more verge on capacity contribution from battery-type energy storage than that in the absence of O_2 (Figure 4F). In addition, the CV curves (Figures S13A and S13B) showed that the oxidation peak threshold position was 1.67 V in the presence of O_2 at 0.2 mV s^{-1} , which appeared later than that in the absence of O_2 (1.63 V). Thus, O_2 participated in the capacity contribution of the α -MnO₂ cathode. The overall reactions for Zn-MnO₂ battery in $ZnSO_4$ electrolyte (in the presence of O_2) can be summarized as the following process during charging and discharging process: $MnO_2 + 1/4O_2 + Zn + (15+4x)/12H_2O + 1/3ZnSO_4 \leftrightarrow MnOOH + 1/3ZnSO_4[Zn(OH)_2]_3 \cdot xH_2O$. The formation of MnOOH indicates a possible, alternative conversion reaction of Zn^{2+} ion intercalation into MnO₂. It is likely that MnO₂ reacts with a proton from water to form MnOOH

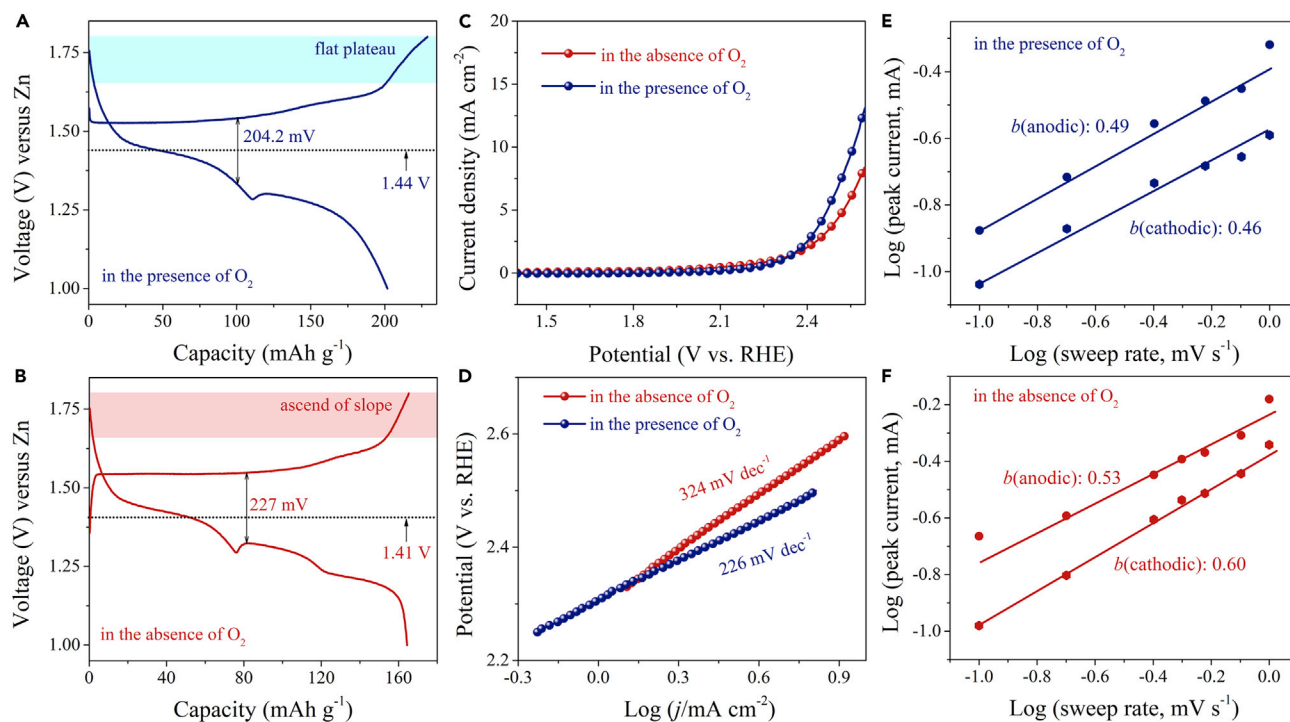


Figure 4. The Effect of O₂ on the Electrochemistry of Zn-MnO₂ Battery

The first GCD curves of Zn-MnO₂ batteries (A) in the presence of O₂ and (B) in absence of O₂ at 0.1 A g⁻¹. Linear sweep voltammetry (LSV) curves (C) and the corresponding Tafel plots (D) of α-MnO₂ electrodes under the three-electrode system in the presence of O₂ and in absence of O₂. The determination of the *b* values of Zn-MnO₂ batteries under the conditions (E) in the presence of O₂ and (F) in absence of O₂.

(MnO₂ + H⁺ + e⁻ ↔ MnOOH). The reaction mechanism is the active conversion reaction between MnO₂ and H⁺. As a result, we can draw a conclusion that the combination of Zn anode and α-MnO₂ cathode in 2 M aqueous ZnSO₄ electrolyte without oxygen presents a high-reversibility and high-cycling-stability aqueous Zn-MnO₂ battery.

Effect of the Dissolved O₂ Exists in Other Types of Aqueous ZIBs

To prove whether the impact of the dissolved O₂ exists in other types of aqueous ZIBs, we constructed other four ZIBs using home-made VO₂, V₂O₅, Na_{0.55}Mn₂O₄·1.5H₂O, and K₂Zn₃[Fe(CN)₆]₂·(H₂O)₉ as cathodes and using 2 M ZnSO₄ solutions in the presence of O₂ and in absence of O₂ as electrolytes. Figures S14–S17, 5A, 5C, 5E, and 5G show the microstructures of the four cathode materials. Importantly, as shown in Figures 5B, 5D, 5F, and 5H, all of the ZIBs showed better cycling stability in the O₂-free environment than those in the presence of O₂. It indicated that such impact of the dissolved oxygen on the cycling stability was general in different types of ZIBs. It should be noted that, among these four ZIBs, Zn-VO₂ battery in the presence of oxygen showed a higher initial capacity than that in the absence of oxygen, which was similar to Zn-MnO₂ battery. It might be attributed to the electrocatalytic activity of VO₂ with oxygen (Wan et al., 2019).

In summary, we studied the electrochemical reversibility of Zn anode and aqueous Zn-MnO₂ battery with the consideration of O₂ dissolved in electrolyte. Zn anode will react with O₂ during cycling process, resulting in the instability of Zn/Zn symmetrical battery. By eliminating O₂ in the electrolyte, the cycling life of Zn/Zn battery can increase more than 20 times. For Zn-MnO₂ battery, the removal of O₂ from the electrolyte can eliminate the oxygen corrosion on Zn anode, thus offering a better energy storage system with a higher capacity retention during cycling. The impact of the dissolved oxygen on the cycling stability also exists in other ZIBs using different cathodes, including VO₂, V₂O₅, Na_{0.55}Mn₂O₄·1.5H₂O, and K₂Zn₃[Fe(CN)₆]₂·(H₂O)₉. The study not only is conducive to understand the electrochemistry of aqueous ZIBs more accurately but also provides useful information to design better aqueous ZIBs by controlling oxygen dissolved in electrolytes.

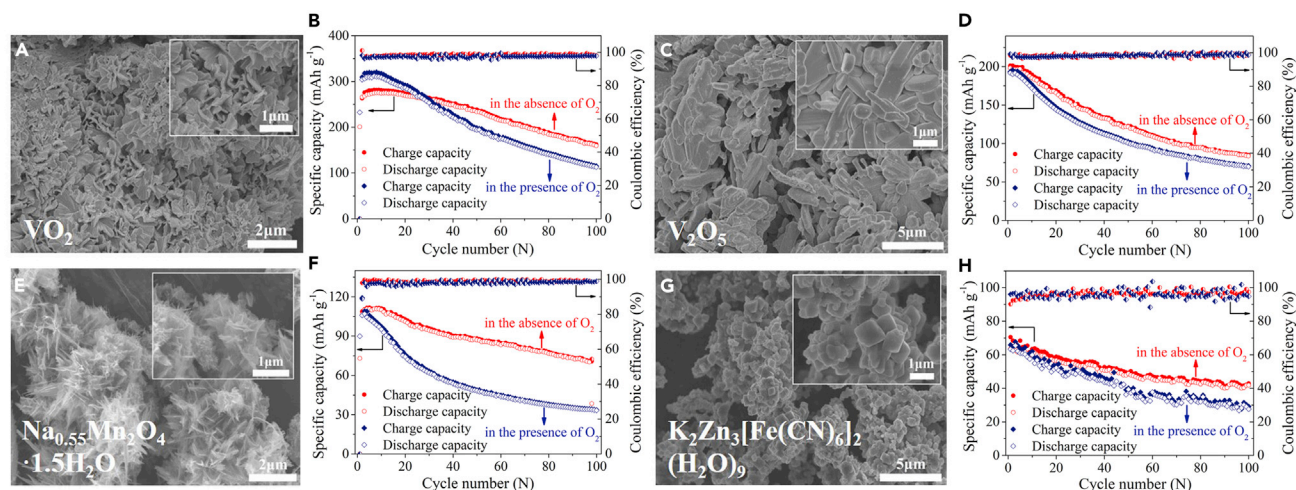


Figure 5. The Impact of the Dissolved O_2 in Aqueous ZIBs with Cathodes of VO_2 , V_2O_5 , $Na_{0.55}Mn_2O_4 \cdot 1.5H_2O$, and $K_2Zn_3[Fe(CN)_6]_2 \cdot (H_2O)_9$ Using the 2 M $ZnSO_4$ Electrolytes in the Presence of O_2 and in Absence of O_2

- (A) SEM characterization of VO_2 .
 (B) Cycling stability of Zn- VO_2 batteries at 0.1 A g^{-1} with a voltage window of 0.2–1.6 V.
 (C) SEM characterization of V_2O_5 .
 (D) Cycling stability of Zn- V_2O_5 batteries at 0.1 A g^{-1} with a voltage window of 0.2–1.6 V.
 (E) SEM characterization of $Na_{0.55}Mn_2O_4 \cdot 1.5H_2O$.
 (F) Cycling stability of Zn- $Na_{0.55}Mn_2O_4 \cdot 1.5H_2O$ batteries at 0.1 A g^{-1} with a voltage window of 1–1.8 V.
 (G) SEM characterization of $K_2Zn_3[Fe(CN)_6]_2 \cdot (H_2O)_9$.
 (H) Cycling stability of Zn- $K_2Zn_3[Fe(CN)_6]_2 \cdot (H_2O)_9$ batteries at 0.1 A g^{-1} with a voltage window of 0.8–1.9 V.

Limitations of the Study

We revealed the impact of oxygen dissolved in electrolytes on aqueous zinc-ion batteries here. The study may need more rigorous analyses and evidence (such as *in-situ* or *in-operando* experiments) for the reaction mechanism of oxygen on zinc-ion batteries.

METHODS

All methods can be found in the accompanying [Transparent Methods supplemental file](#).

DATA AND CODE AVAILABILITY

The data that support the findings of this study are available from the corresponding author upon reasonable request.

SUPPLEMENTAL INFORMATION

Supplemental Information can be found online at <https://doi.org/10.1016/j.isci.2020.100995>.

ACKNOWLEDGMENTS

This work was supported by the National Natural Science Foundation of China, China (21673263 and 21805292), One-Three-Five Strategic Planning of Chinese Academy of Sciences (CAS), and the DNL Cooperation Fund, CAS (DNL180307).

AUTHOR CONTRIBUTIONS

X.B.Y. designed this work; L.J.S. carried out the materials synthesis and electrochemical experiments; X.B.Y. and L.J.S. wrote the paper and analyzed the results. L.Y.L, B.L., and J.N.M. contributed to the discussion of the results. All authors wrote the manuscript, read, and approved the final manuscript.

DECLARATION OF INTERESTS

The authors declare no competing interests.

Received: January 14, 2020

Revised: March 11, 2020

Accepted: March 15, 2020

Published: April 24, 2020

REFERENCES

- Abdallah, M. (2003). Ethoxylated fatty alcohols as corrosion inhibitors for dissolution of zinc in hydrochloric acid. *Corros. Sci.* 45, 2705–2716.
- Abdelall, M.S., Ahmed, Z.A., and Hassan, M.S. (1992). Inhibiting and accelerating effects of some quinolines on the corrosion of zinc and some binary zinc alloys in HCl solution. *J. Appl. Electrochem.* 22, 1104–1109.
- Alfaruqi, M.H., Gim, J., Kim, S., Song, J., Jo, J., Kim, S., Mathew, V., and Kim, J. (2015a). Enhanced reversible divalent zinc storage in a structurally stable α -MnO₂ nanorod electrode. *J. Power Sourc.* 288, 320–327.
- Alfaruqi, M.H., Mathew, V., Gim, J., Kim, S., Song, J., Baboo, J.P., Choi, S.H., and Kim, J. (2015b). Electrochemically induced structural transformation in a γ -MnO₂ cathode of a high capacity zinc-ion battery system. *Chem. Mater.* 27, 3609–3620.
- Ballesteros, J., Díaz-Arista, P., Meas, Y., Ortega, R., and Trejo, G. (2007). Zinc electrodeposition in the presence of polyethylene glycol 20000. *Electrochim. Acta* 52, 3686–3696.
- Benson, B.B., Krause, D., Jr., and Peterson, M.A. (1979). The solubility and isotopic fractionation of gases in dilute aqueous solution. I. Oxygen. *J. Sol. Chem.* 8, 655–690.
- Boeun, L., Hae, R. L., Haesik, K., Kyung, Yoon C., Byung, Won, C., and Hyoung, O.S. (2015). Elucidating the intercalation mechanism of zinc ions into α -MnO₂ for rechargeable zinc batteries. *Chem. Commun.* 51, 9265–9268.
- Chao, D., Zhou, W., Ye, C., Zhang, Q., Chen, Y., Gu, L., Davey, K., and Qiao, S.Z. (2019). An electrolytic Zn–MnO₂ battery for high-voltage and scalable energy storage. *Angew. Chem. Int. Ed.* 58, 7823–7828.
- Chao, D., Zhu, C., Song, M., Liang, P., Zhang, X., Tiep, N.H., Zhao, H., Wang, J., Wang, R., and Zhang, H. (2018). A high-rate and stable quasi-solid-state zinc-ion battery with novel 2D layered zinc orthovanadate array. *Adv. Mater.* 30, 1803181.
- Chen, L., Yan, M., Mei, Z., and Mai, L. (2017). Research progress and prospect of aqueous zinc ion battery. *J. Inorg. Mater.* 32, 225–234.
- Chiasserini, C.F., and Rao, R.R. (2000). Energy efficient battery management. *IEEE J. Sel. Area. Commun.* 19, 1235–1245.
- Davis, R.E., Horvath, G.L., and Tobias, C.W. (1967). The solubility and diffusion coefficient of oxygen in potassium hydroxide solutions. *Electrochim. Acta* 12, 287–297.
- Diggle, J.W., and Damjanovic, A. (1972). The inhibition of the dendritic electrocrystallization of zinc from doped alkaline zincate solutions. *J. Electrochem. Soc.* 119, 1649–1658.
- Fang, G., Zhou, J., Pan, A., and Liang, S. (2018). Recent advances in aqueous zinc-ion batteries. *ACS Energy Lett.* 3, 2480–2501.
- Hu, X., Murgovski, N., Johannesson, L., and Bo, E. (2013). Energy efficiency analysis of a series plug-in hybrid electric bus with different energy management strategies and battery sizes. *Appl. Energy* 117, 1001–1009.
- Jin, Y., Zou, L., Liu, L., Engelhard, M.H., Patel, R.L., Nie, Z., Han, K.S., Shao, Y., Wang, C., and Zhu, J. (2019). Joint charge storage for high-rate aqueous zinc–manganese dioxide batteries. *Adv. Mater.* 31, 1900567.
- Lan, C., Lee, C., and Chin, T. (2007). Tetra-alkyl ammonium hydroxides as inhibitors of Zn dendrite in Zn-based secondary batteries. *Electrochim. Acta* 52, 5407–5416.
- Lee, B., Yoon, C.S., Lee, H.R., Chung, K.Y., Cho, B.W., and Oh, S.H. (2014). Electrochemically-induced reversible transition from the tunneled to layered polymorphs of manganese dioxide. *Sci. Rep.* 4, 6066.
- Lee, B., Seo, H.R., Lee, H.R., Yoon, C.S., Kim, J.H., Chung, K.Y., Cho, B.W., and Oh, S.H. (2016). Critical role of pH evolution of electrolyte in the reaction mechanism for rechargeable zinc batteries. *ChemSusChem* 9, 2948–2956.
- Luo, J.Y., Cui, W.J., He, P., and Xia, Y.Y. (2010). Raising the cycling stability of aqueous lithium-ion batteries by eliminating oxygen in the electrolyte. *Nat. Chem.* 2, 760–765.
- Ma, L., Chen, S., Pei, Z., Li, H., Wang, Z., Liu, Z., Tang, Z., Zapien, J.A., and Zhi, C. (2018). Flexible waterproof rechargeable hybrid zinc batteries initiated by multifunctional oxygen vacancies-rich cobalt oxide. *ACS Nano* 12, 8597–8605.
- Mackinnon, D., Brannen, J., and Fenn, P. (1987). Characterization of impurity effects in zinc electrowinning from industrial acid sulphate electrolyte. *J. Appl. Electrochem.* 17, 1129–1143.
- MacKinnon, D., Morrison, R., Mouland, J., and Warren, P. (1990). The effects of antimony and glue on zinc electrowinning from Kidd Creek electrolyte. *J. Appl. Electrochem.* 20, 728–736.
- Mainar, A.R., Iruin, E., Colmenares, L.C., Kvasha, A., de Meaza, I., Bengoechea, M., Leonet, O., Boyano, I., Zhang, Z., and Blazquez, J.A. (2018). An overview of progress in electrolytes for secondary zinc-air batteries and other storage systems based on zinc. *J. Energy Storage* 15, 304–328.
- Mathew, V., Xiu, Z., Alfaruqi, M.H., Gim, J., Kim, S., Song, J., Thi, T.V., Tung, D.P., Baboo, J.P., and Kim, J. (2015). A structurally stable α -MnO₂ nanorod cathode for enhanced reversible divalent zinc storage. *ECS Meet. Abstr.* 3, 287.
- Mondoloni, C., Laborde, M., Rioux, J., Andoni, E., and Levy-Clement, C. (1992). Rechargeable alkaline manganese dioxide batteries. I. In situ x-ray diffraction investigation of the H⁺/ γ -MnO₂ (EMD-Type) insertion system. *J. Electrochem. Soc.* 139, 954–959.
- Pan, C., Zhang, R., Nuzzo, R.G., and Gewirth, A.A. (2018). ZnNi_xMn_xCo_{2-2x}O₄ spinel as a high-voltage and high-capacity cathode material for nonaqueous Zn-ion batteries. *Adv. Energy Mater.* 8, 1800589.
- Pan, H., Shao, Y., Yan, P., Cheng, Y., Han, K.S., Nie, Z., Wang, C., Yang, J., Li, X., and Bhattacharya, P. (2016). Reversible aqueous zinc/manganese oxide energy storage from conversion reactions. *Nat. Energy* 1, 1–7.
- Parker, J.F., Chervin, C.N., Pala, I.R., Machler, M., Burz, M.F., Long, J.W., and Rolison, D.R. (2017). Rechargeable nickel-3D zinc batteries: an energy-dense, safer alternative to lithium-ion. *Science* 356, 415–418.
- Pei, A., Zheng, G., Shi, F., Li, Y., and Cui, Y. (2017). Nanoscale nucleation and growth of electrodeposited lithium metal. *Nano Lett.* 17, 1132–1139.
- Pendashteh, A., Sanchez, J.S., Palma, J., Anderson, M., and Marcilla, R. (2019). Anchored NiCoMnS₄ nanoparticles on N-doped rGO: high-performance bifunctional electrocatalysts for rechargeable Zn–Air batteries. *Energy Storage Mater.* 20, 216–224.
- Shinde, S.S., Lee, C.H., Jung, J.-Y., Wagh, N.K., Kim, S.-H., Kim, D.-H., Lin, C., Lee, S.U., and Lee, J.-H. (2019). Unveiling dual-linkage 3D hexaiminobenzene metal–organic frameworks towards long-lasting advanced reversible Zn–air batteries. *Energy Environ. Sci.* 12, 727–738.
- Simunic, T., Benini, L., and Micheli, G.D. (2001). Energy-efficient design of battery-powered embedded systems. *IEEE T. VLSI Syst.* 9, 15–28.
- Song, M., Tan, H., Chao, D., and Fan, H.J. (2018). Recent advances in Zn-ion batteries. *Adv. Funct. Mater.* 28, 1802564.
- Stupnisek-Lisac, E., Kasunic, D., and Vorkapic-Furac, J. (1995). Imidazole derivatives as corrosion inhibitors for zinc in hydrochloric acid. *Corrosion* 51, 767–772.
- Sun, W., Wang, F., Hou, S., Yang, C., Fan, X., Ma, Z., Gao, T., Han, F., Hu, R., and Zhu, M. (2017). Zn/MnO₂ battery chemistry with H⁺ and Zn²⁺ coinsertion. *J. Am. Chem. Soc.* 139, 9775–9778.
- Trejo, G., Ruiz, H., Borges, R.O., and Meas, Y. (2001). Influence of polyethoxylated additives on zinc electrodeposition from acidic solutions. *J. Appl. Electrochem.* 31, 685–692.

- Tripathy, B., Das, S., Hefter, G., and Singh, P. (1997). Zinc electrowinning from acidic sulfate solutions: Part I: effects of sodium lauryl sulfate. *J. Appl. Electrochem.* *27*, 673–678.
- Trócoli, R., and La Mantia, F. (2015). An aqueous zinc-ion battery based on copper hexacyanoferrate. *ChemSusChem* *8*, 481–485.
- Wan, F., Zhang, L., Dai, X., Wang, X., Niu, Z., and Chen, J. (2018). Aqueous rechargeable zinc/sodium vanadate batteries with enhanced performance from simultaneous insertion of dual carriers. *Nat. Commun.* *9*, 1656.
- Wan, F., Zhang, Y., Zhang, L., Liu, D., Wang, C., Song, L., Niu, Z., and Chen, J. (2019). Reversible oxygen redox chemistry in aqueous zinc-ion batteries. *Angew. Chem. Int. Ed.* *58*, 7062–7067.
- Wang, J., Zhang, L., Zhang, C., and Zhang, J. (2001). Effects of bismuth ion and tetrabutylammonium bromide on the dendritic growth of zinc in alkaline zincate solutions. *J. Power Sources* *102*, 139–143.
- Wang, R., Kirk, D., and Zhang, G. (2006). Effects of deposition conditions on the morphology of zinc deposits from alkaline zincate solutions. *J. Electrochem. Soc.* *153*, C357–C364.
- Xu, C., Li, B., Du, H., and Kang, F. (2012). Energetic zinc ion chemistry: the rechargeable zinc ion battery. *Angew. Chem. Int. Ed.* *51*, 933–935.
- Yang, Q., Liang, G., Guo, Y., Liu, Z., Yan, B., Wang, D., Huang, Z., Li, X., Fan, J., and Zhi, C. (2019). Do zinc dendrites exist in neutral zinc batteries: a developed electrohealing strategy to in situ rescue in-service batteries. *Adv. Mater.* *31*, 1903778.
- Yang, Y., Tang, Y., Fang, G., Shan, L., Guo, J., Zhang, W., Wang, C., Wang, L., Zhou, J., and Liang, S. (2018). Li⁺ intercalated V₂O₅·nH₂O with enlarged layer spacing and fast ion diffusion as an aqueous zinc-ion battery cathode. *Energy Environ. Sci.* *11*, 3157–3162.
- Yi, J., Liang, P., Liu, X., Wu, K., Liu, Y., Wang, Y., Xia, Y., and Zhang, J. (2018). Challenges, mitigation strategies and perspectives in development of zinc-electrode materials and fabrication for rechargeable zinc–air batteries. *Energy Environ. Sci.* *11*, 3075–3095.
- Zhang, L., Chen, L., Zhou, X., and Liu, Z. (2015). Toward high-voltage aqueous metal-ion batteries beyond 1.5 V: the zinc/zinc hexacyanoferrate system. *Adv. Energy Mater.* *5*, 1400930.
- Zhang, Q., and Hua, Y. (2009). Effects of 1-butyl-3-methylimidazolium hydrogen sulfate-[BMIM]HSO₄ on zinc electrodeposition from acidic sulfate electrolyte. *J. Appl. Electrochem.* *39*, 261.
- Zhang, W., Duan, D., and Yang, L. (2011). Relay selection from a battery energy efficiency perspective. *IEEE T. Commun.* *59*, 1525–1529.
- Zhao, J., Zhang, J., Yang, W., Chen, B., Zhao, Z., Qiu, H., Dong, S., Zhou, X., Cui, G., and Chen, L. (2019a). “Water-in-deep eutectic solvent” electrolytes enable zinc metal anodes for rechargeable aqueous batteries. *Nano Energy* *57*, 625–634.
- Zhao, Z., Zhao, J., Hu, Z., Li, J., Li, J., Zhang, Y., Wang, C., and Cui, G. (2019b). Long-life and deeply rechargeable aqueous Zn anodes enabled by a multifunctional brightener-inspired interphase. *Energy Environ. Sci.* *12*, 1938–1949.
- Zheng, J., Zhao, Q., Tang, T., Yin, J., Quilty, C.D., Renderos, G.D., Liu, X., Deng, Y., Wang, L., Bock, D.C., et al. (2019). Reversible epitaxial electrodeposition of metals in battery anodes. *Science* *366*, 645–648.

iScience, Volume 23

Supplemental Information

Revealing the Impact of Oxygen

Dissolved in Electrolytes

on Aqueous Zinc-Ion Batteries

Lijun Su, Lingyang Liu, Bao Liu, Jianing Meng, and Xingbin Yan

Transparent Methods

Material Synthesis

α -MnO₂ was synthesized by a typical method,(Pan et al., 2016) 2 mL 0.5 M H₂SO₄ and 0.003 M MnSO₄·H₂O were added to 90 mL deionized water. And 20 mL 0.1 M KMnO₄ was slowly added into the above mixed solution. The mixture was magnetically stirred for 2 h. Then, the mixed solution was transferred to a Teflon-lined autoclave and heated at 120 °C for 12 h. The obtained products were collected by centrifugation, washed three times with water, and dried by a vacuum oven at room temperature.

The Na_{0.55}Mn₂O₄·1.5H₂O were synthesized by the molten salts method.(Hu et al., 2017) 5 g NaNO₃ was added into a crucible and then transferred to the muffle furnace at a temperature of 350 °C for 10 minutes. After NaNO₃ became molten state completely, 0.2 g MnSO₄ was added into the molten salt and heated for 1 minute. Then, the reaction product was taken out from the muffle furnace and cooled to room temperature. The final product was washed by deionized water and dried at room temperature.

V₂O₅ was synthesized as follows:(Zhang et al., 2018) commercial graphite and commercial V₂O₅ powder with a mass ratio of 2:8 were added into a hard steel ball-milled jar. The mixture was ball milled in a ball miller at 400 rpm for 180 minutes.

VO₂ was synthesized by a typical fabrication,(Ding et al., 2018) 1.8 g H₂C₂O₄·2H₂O and 1.2 g V₂O₅ were added into 40 mL deionized water, and the above mixed solution was reacted at 75 °C for 60 minutes. Then, the above dispersion was transferred into a Teflon-lined autoclave and heated at 180 °C for 180 minutes. Finally, the product was collected and washed with ethanol and deionized water and frozen-drying for 12 h.

$\text{K}_2\text{Zn}_3[\text{Fe}(\text{CN})_6]_2 \cdot (\text{H}_2\text{O})_9$ was synthesized via the following method:(Zhang et al., 2015) 100 mL 0.05 M $\text{K}_3\text{Fe}(\text{CN})_6$ and 100 mL 0.1 M ZnSO_4 were added into 50 mL H_2O under vigorous stirring at 60 °C. After reaction, the suspensions were left to stand for several hours. Finally, the obtained powder was filtered, washed with deionized water, then dried at 70 °C.

Characterizations

The crystalline structure of the as-obtained material was characterized by powder X-ray diffraction pattern (XRD, Rigaku D/Max-2400, Cu-K α radiation, $\lambda = 0.15405$ nm). Surface morphology and microstructure were investigated through field emission scanning electron microscope (FESEM, JSM 6701F), transmission electron microscope (TEM, JEOL 2100 FEG), high-resolution TEM (HRTEM, JOEL, JEM-2010 F) and atomic force microscope (AFM, MultiMode 8).

Electrochemical measurements

Oxygen evolution reaction (OER) test was performed in three-electrode system under the program of linear sweep voltammetry (LSV) with a scan rate of 5 mV s⁻¹ and a voltage window of 0 to 1.8 V. The glassy carbon electrode was used as the working electrode, the saturated calomel electrode as the reference electrode and a platinum electrode as the counter electrode.

Corrosion test and cyclic voltammetry (CV) were carried on an electrochemical workstation (CHI660D, Chenhua, Shanghai, China). Linear polarization and chronoamperograms (CAs) measurements were conducted in a three-electrode configuration, in which bare Zn was used as the working electrode, Zn plate as the

counter, and saturated calomel (SCE) as the reference electrodes, respectively. The corrosion potential and corrosion current were calculated from Tafel plots. Electrochemical impedance spectrum (EIS) were recorded on the electrochemical workstation with a frequency range from 1 MHz to 0.01 Hz. Galvanostatic charge-discharge (GCD) measurements were performed with a battery test system (Land CT2001A model, Wuhan Land Electronics Ltd.). And the energy efficiency data of the symmetrical Zn/Zn battery was obtained directly from LAND system.

Fabrication of coin cells: The positive electrodes comprised active material powder (80 wt%), conductive graphite (10 wt%) and carboxymethylcellulose (CMC) (10 wt%). The active material could be the one of α -MnO₂, Na_{0.55}Mn₂O₄·1.5H₂O, VO₂, V₂O₅ or K₂Zn₃[Fe(CN)₆]₂·(H₂O)₉. The mass loading for the cathode materials was about 1 mg cm⁻² on the stainless-steel grid current collector. The anode electrodes were Zn plates of 1×1 cm⁻². Each battery was assembled into a coin cell with a glass fiber as the separator and the 2 M ZnSO₄ as the aqueous electrolyte. Specifically, coin cells were assembled in different atmosphere: in an open laboratory atmosphere (dissolved O₂ content was 6.24 mg L⁻¹), in the presence of O₂ (dissolved O₂ content was 9.17 mg L⁻¹) and in the absence of O₂ (dissolved O₂ content was less than 0.1 mg L⁻¹).

Supplemental Figures

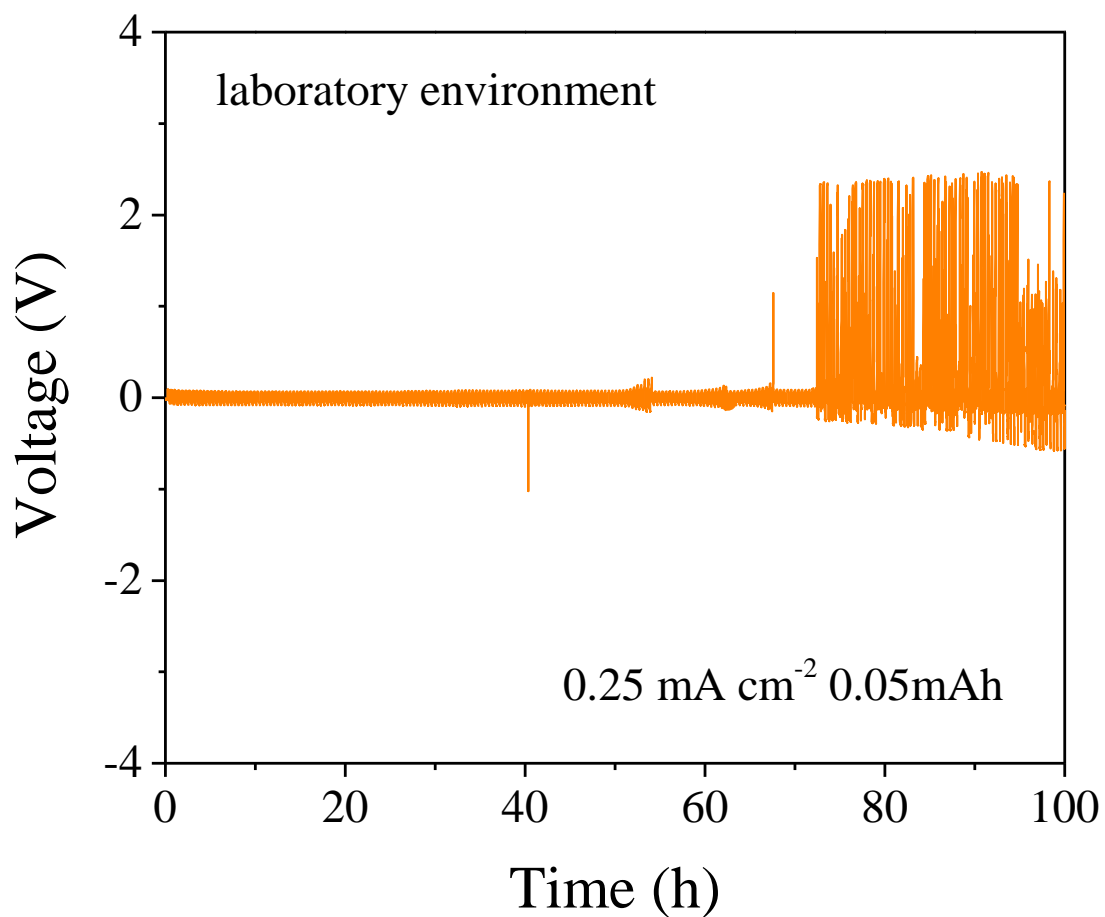


Figure S1. Characterization of Zn/Zn cell, related to Figure 1.

Electrochemical stability and reversibility of the symmetrical Zn/Zn cell using 2 M ZnSO₄ aqueous electrolyte in open laboratory environment at a current density of 0.25 mA cm⁻² and a charge/discharge cut-off capacity of 0.05 mAh.

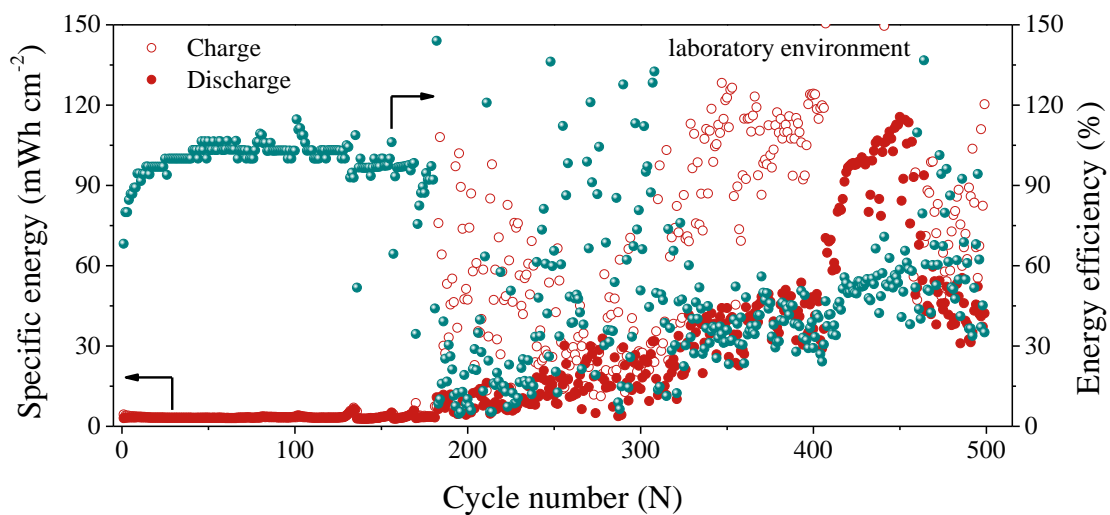


Figure S2. Characterization of Zn/Zn cell, related to Figure 1.

The specific energy and energy efficiency of the symmetrical Zn/Zn cell in open laboratory environment.

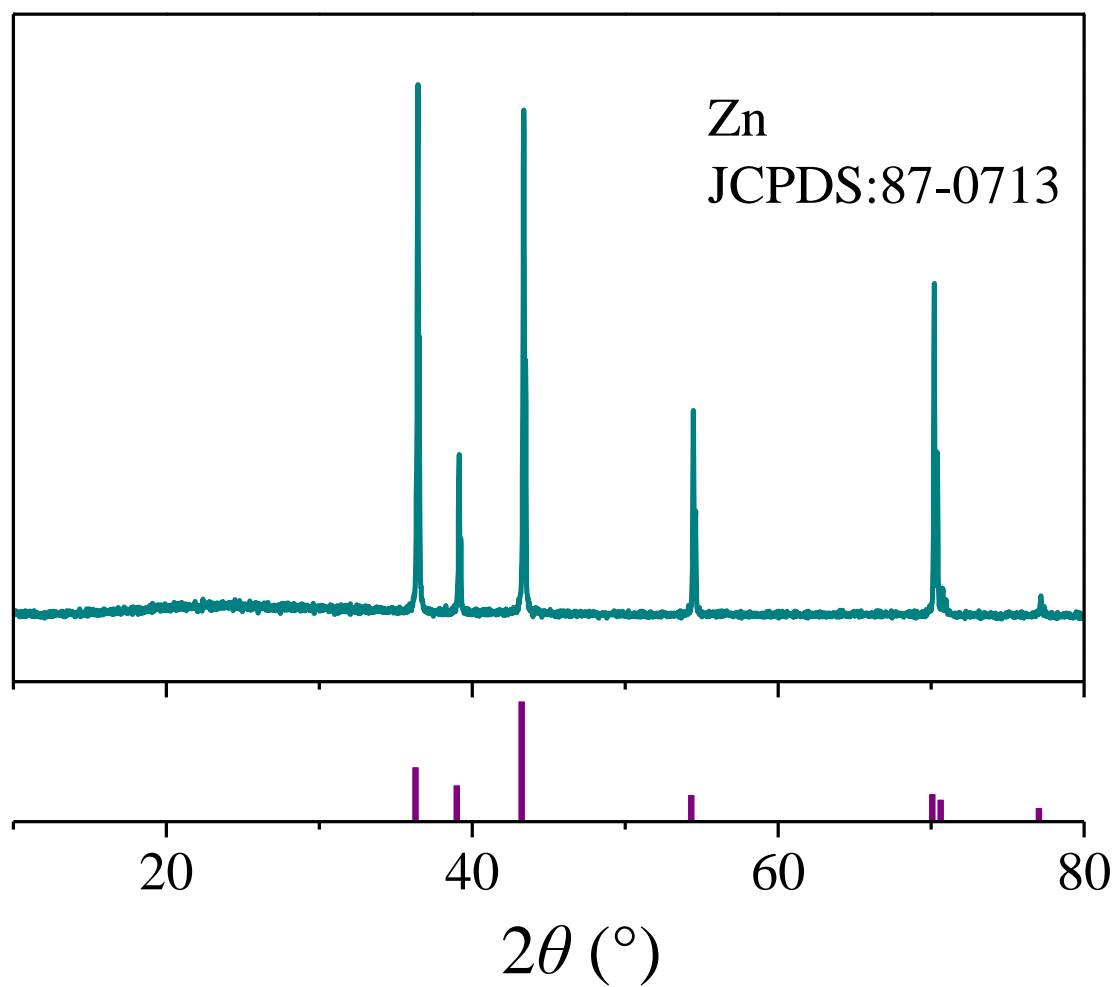


Figure S3. Characterization of Zn, related to Figure 2.

XRD pattern of pristine Zn plate.

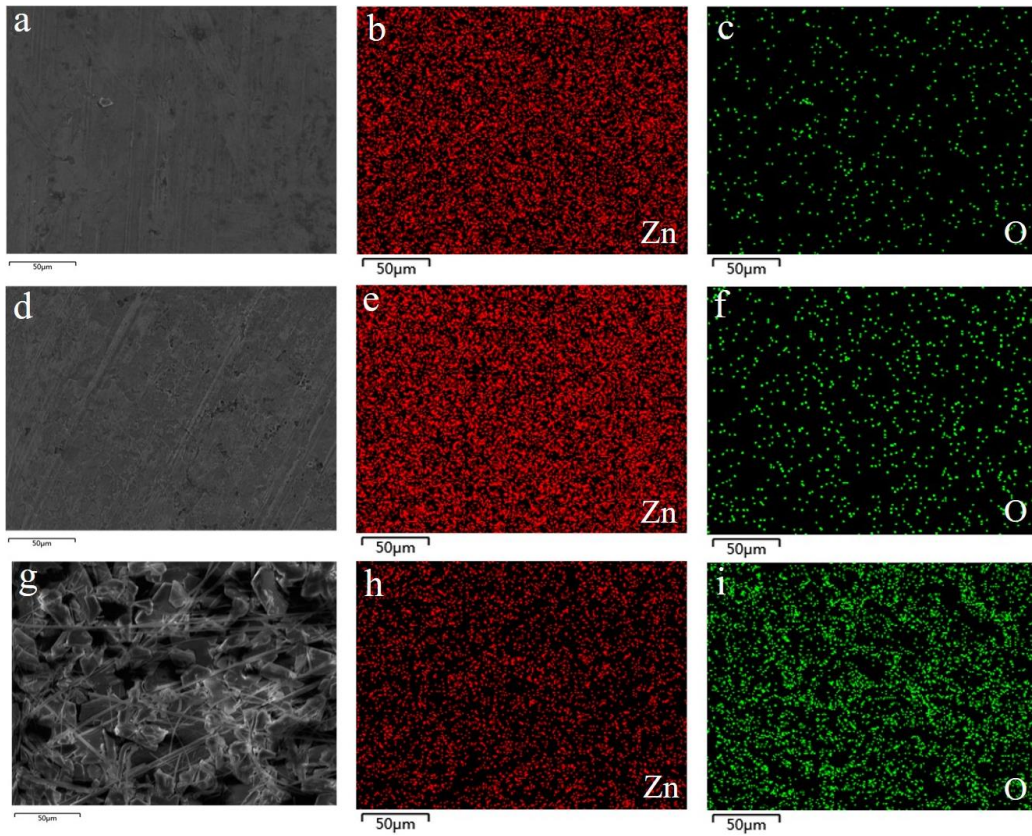


Figure S4. Characterization of Zn, related to Figure 2.

SEM as well as element mapping images of Zn. (a-c) Pristine Zn plate, (d-f) Zn plate after galvanostatic cycling for 120 h in the absence of O_2 , (g-i) Zn plate after galvanostatic cycling for 120 h in the presence of O_2 .

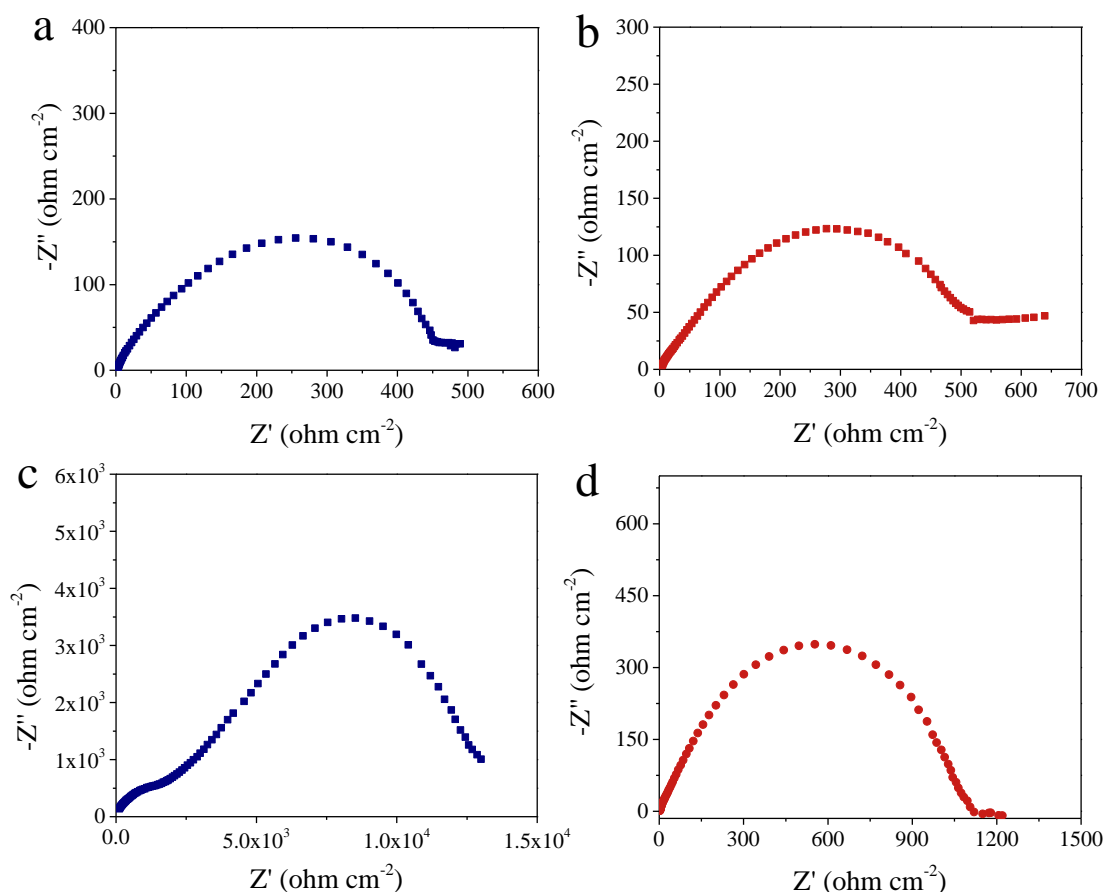


Figure S5. Impedance study of Zn/Zn cells, related to Figure 2.

EIS plots of symmetric Zn/Zn cells. EIS plots of pristine symmetric Zn/Zn cells in the presence of O₂ (a) and in absence of O₂ (b). (c) EIS plot of symmetric Zn/Zn cell after galvanostatic cycling for 30 h in the presence of O₂. (d) EIS plot of symmetric Zn/Zn cell after galvanostatic cycling for 500 h in the absence of O₂.

EIS plots showed that the initial symmetric Zn/Zn batteries assembled in the presence of O₂ (Figure S5a) and in absence of O₂ (Figure S5b) exhibited small electrochemical impedance. In the presence of O₂, the impedance of the symmetric Zn/Zn battery significantly increased by 100 orders of magnitude after galvanostatic cycling for 30 h (Figure S5c). It indicated that the surface of Zn was corroded, which caused electron insulation on the surface of Zn. When the dissolved O₂ was removed, the internal

corrosion of the battery was greatly reduced. After cycling for 120 h (Figure 2b), the electrochemical impedance increased slightly compared with that of the initial symmetric Zn/Zn battery before cycling, indicating the internal stability of the battery. As shown in Figure S5d, after cycling 500 h, the electrochemical impedance slightly increased due to the slow corrosion of Zn.

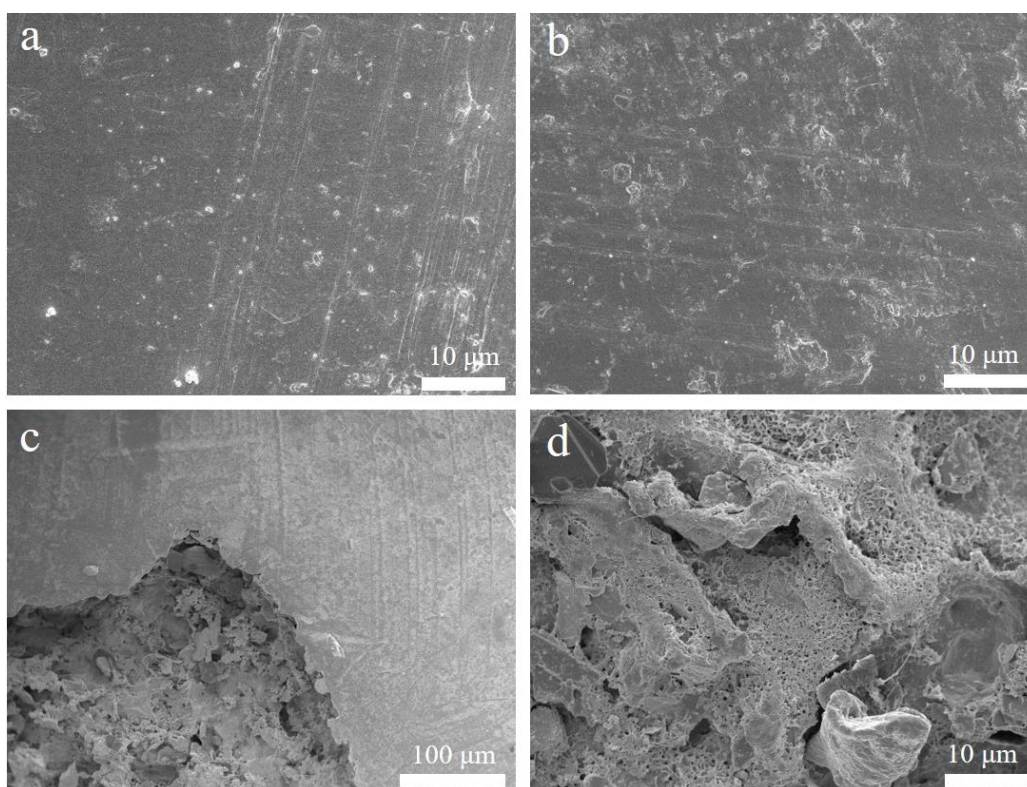


Figure S6. Morphologies of Zn, related to Figure 2.

SEM images of Zn plate. (a) Pristine Zn plate. Zn plates after galvanostatic cycling for 120 h (b) in the absence of O₂ and (c, d) in presence of O₂.

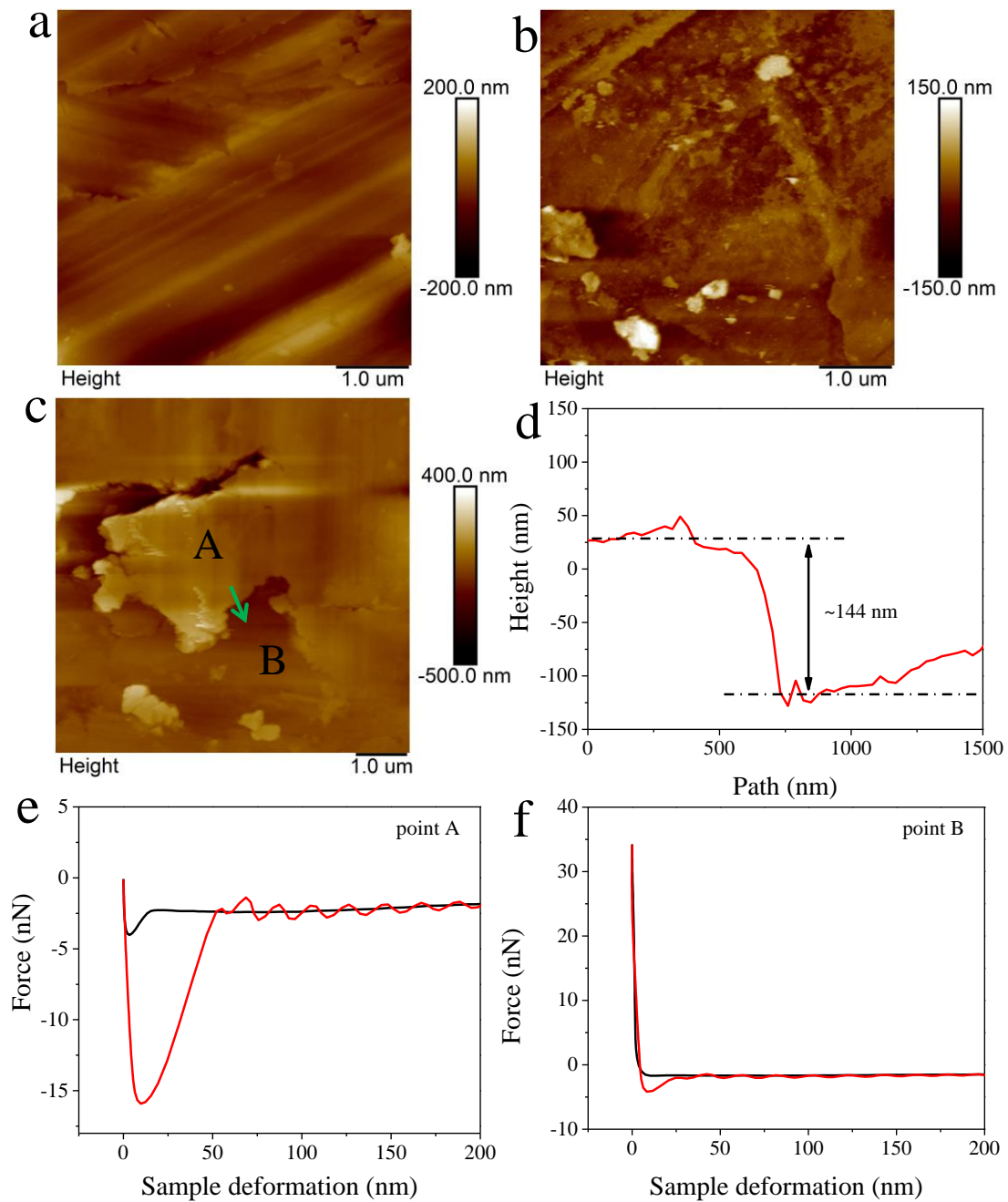


Figure S7. Morphologies of Zn, related to Figure 2.

AFM characterization. (a) Pristine Zn plate, Zn plates after galvanostatic cycling for 120 h in the absence of O₂ (b) and in presence of O₂ (c). (d) The corresponding section height curve of the green line in (c). Indentation curves of Zn plate at point A (e) and B (f).

For the AFM measurement, the pristine Zn surface showed a metal stripe structure

before cycling (Figure S7a). As shown in Figure S7b, there was no serious corrosion on the surface of Zn after cycling 120 h in the absence of O₂ (there was a bits of Zn dendrite), but the flatness of the surface of Zn slightly changed. This was due to the slight corrosion on the surface of Zn. However, as shown in Figure S7c, the surface of Zn was severely corroded after cycling for 120 h in the presence of O₂. The corresponding section height curve showed that the corrosion depth was about 144 nm (Figure S7d). As shown in Figure S7c, point A was the surface of Zn that was not severely corroded and point B was the surface of severely corroded Zn. In addition, the mechanical properties of point A and point B was measured.(Shen et al., 2019) The penetration depth of the probe at point A (Figure S7e) was significantly higher than point B (Figure S7f). The corresponding peak force and the reduced modulus of Zn plate in the presence of O₂ were shown in Table S2. The modulus at point B of the corrosion region was significantly higher than that at point A, which was about one order of magnitude higher. It further reflected that O₂ accelerated the corrosion on the Zn surface, thereby generating some by-products such as zinc oxide, zinc hydroxide and zincate.

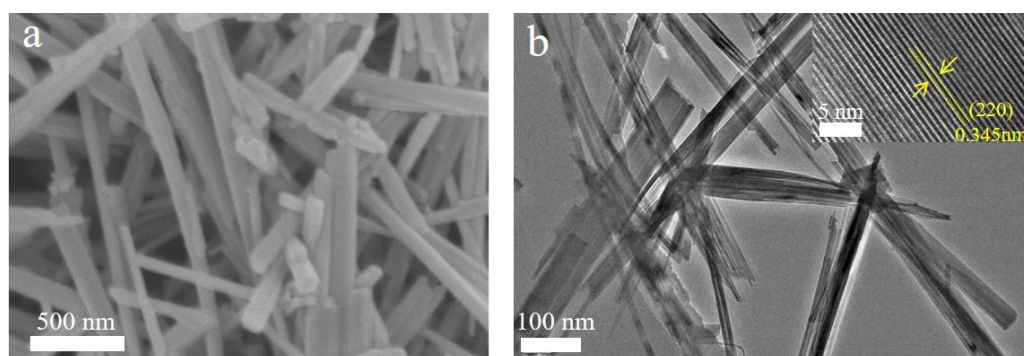


Figure S8. Characterization of α -MnO₂, related to Figure 3.

Structural characterization of α -MnO₂. (a) SEM image. (b) TEM characterization, and the inset is HRTEM image.

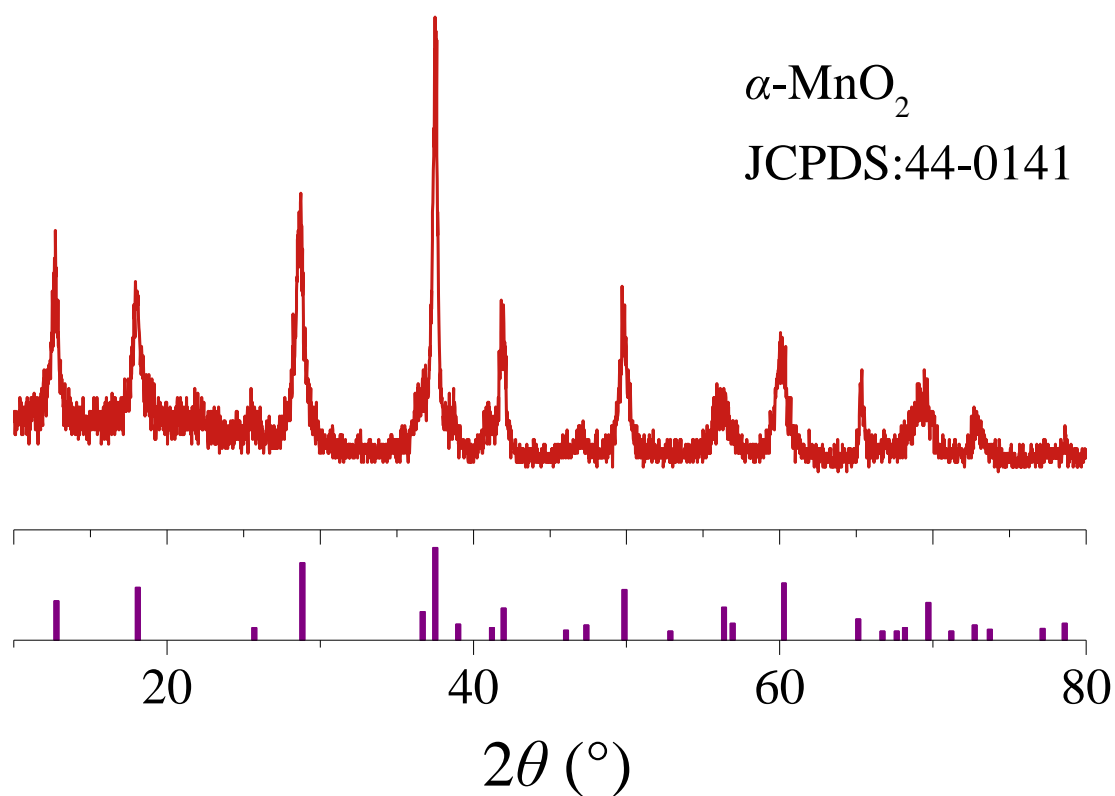


Figure S9. Characterization of α -MnO₂, related to Figure 3.

XRD data of α -MnO₂.

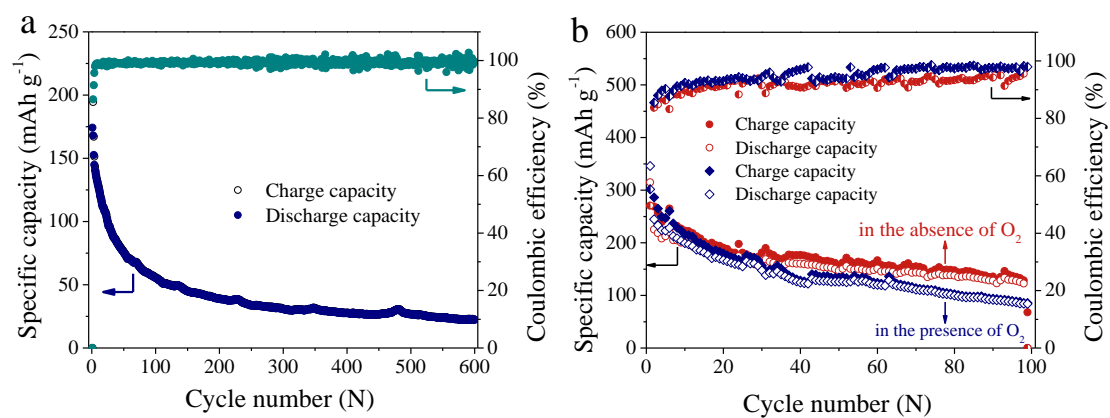


Figure S10. Electrochemical study of Zn/MnO₂ batteries, related to Figure 3.

(a) The cycling performance of the aqueous Zn/MnO₂ battery using 2 M ZnSO₄ electrolyte in the open laboratory environment (the content of dissolved O₂ was 6.24 mg L⁻¹) at 1C (0.308 A g⁻¹). (b) Cycling stability test of the aqueous Zn/MnO₂ batteries using 2 M ZnSO₄ electrolytes in the presence of O₂ and in absence of O₂ at 0.1 A g⁻¹ with voltage window of 1~1.9 V.

When the voltage window of Zn-MnO₂ battery was limited within 1~1.8 V, there will be less oxygen generated via OER at the cathode side. Even though we have verified the α -MnO₂ electrode exhibited a smaller overpotential (58 mV) at 5 mA cm⁻² in the presence of O₂ than that in the absence of O₂, but the LSV characterization indicated that, the oxygen evolution reaction (OER) catalytic activity of the α -MnO₂ was unsatisfactory when compared to some typically reported OER catalysts. As for the long-term difference whether eliminate oxygen or not, we have extended the voltage window of the Zn-MnO₂ battery of 1~1.9 V, thus, the cycling stability test of the aqueous Zn/MnO₂ batteries using 2 M ZnSO₄ electrolytes in the presence of O₂ and in absence of O₂ at 0.1 A g⁻¹ can be compared as shown in Figure S10. The corresponding Zn-MnO₂ battery exhibited a faster capacity attenuation in the O₂-rich environment. The results proved that the existence of dissolved O₂ indeed resulted in the corrosion of Zn anode, and thus aggravated the capacity decay of the Zn-MnO₂ battery.

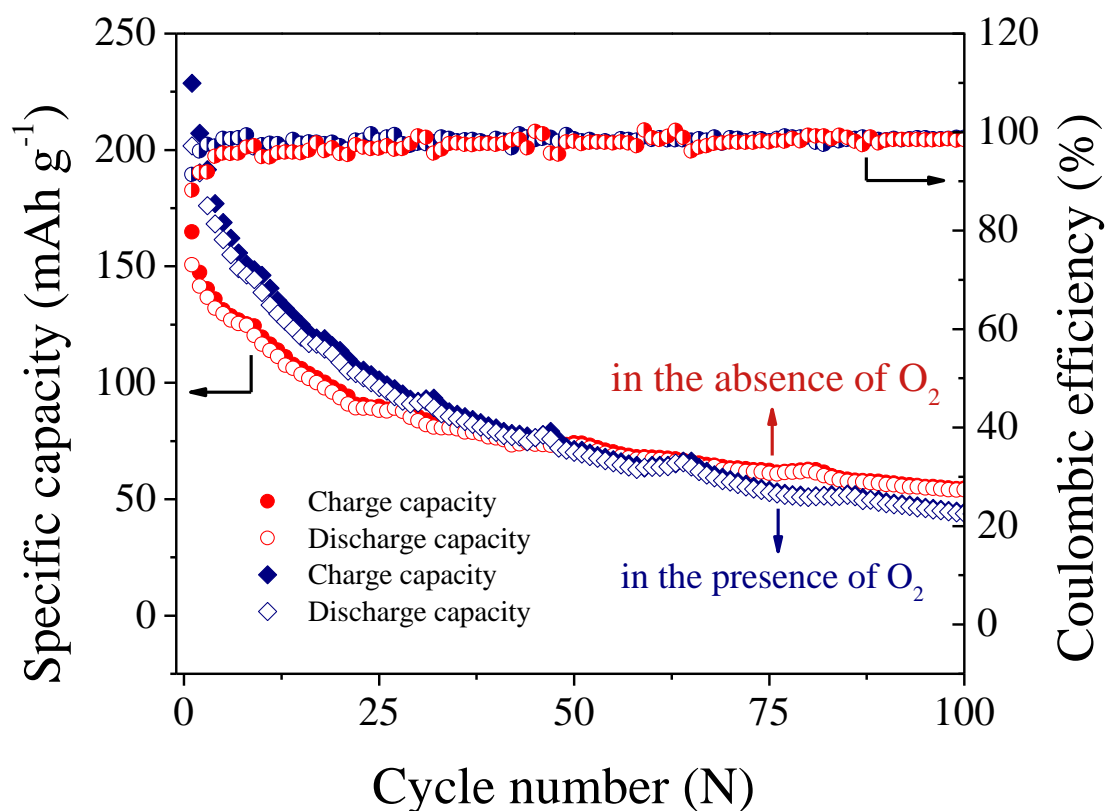


Figure S11. Electrochemical study of Zn/MnO₂ battery, related to Figure 3.

Cycling stability test of the aqueous Zn/MnO₂ batteries using 2 M ZnSO₄ electrolytes in the presence of O₂ and in absence of O₂ at 0.1 A g⁻¹ without adding conductive graphite of cathode material.

We have compared the cycling stability of aqueous Zn/MnO₂ batteries using 2 M ZnSO₄ electrolytes in the presence of O₂ and in absence of O₂ at 0.1 A g⁻¹ without adding conductive graphite of cathode material (Figure S11). A high reversible capacity was delivered in the first cycle in the presence of oxygen. Thus, the extra charge capacity was not due to the oxidation of conductive graphite.

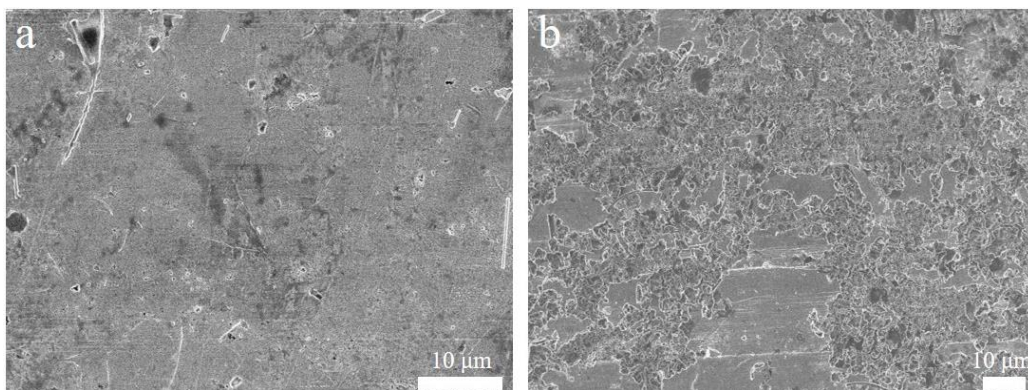


Figure S12. Characterization of Zn, related to Figure 3.

SEM images of Zn anodes for the aqueous Zn/MnO₂ batteries after cycling test (corresponding to Figure 3a) in the absence of O₂ (a) and in presence of O₂ (b).

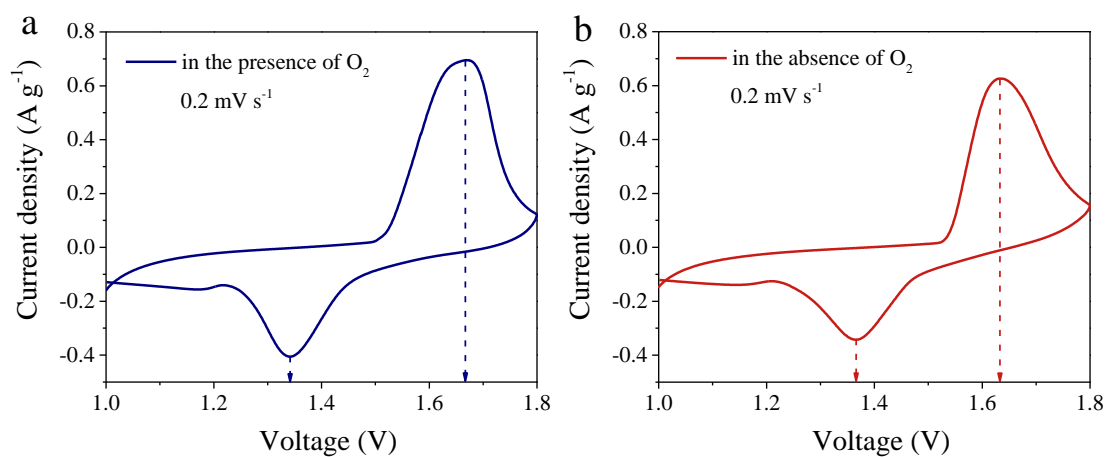


Figure S13. Electrochemical study of Zn/MnO₂ batteries, related to Figure 4.

CV curves of aqueous Zn/MnO₂ batteries at 0.2 mV s⁻¹ in the presence (a) and in absence of O₂ (b).

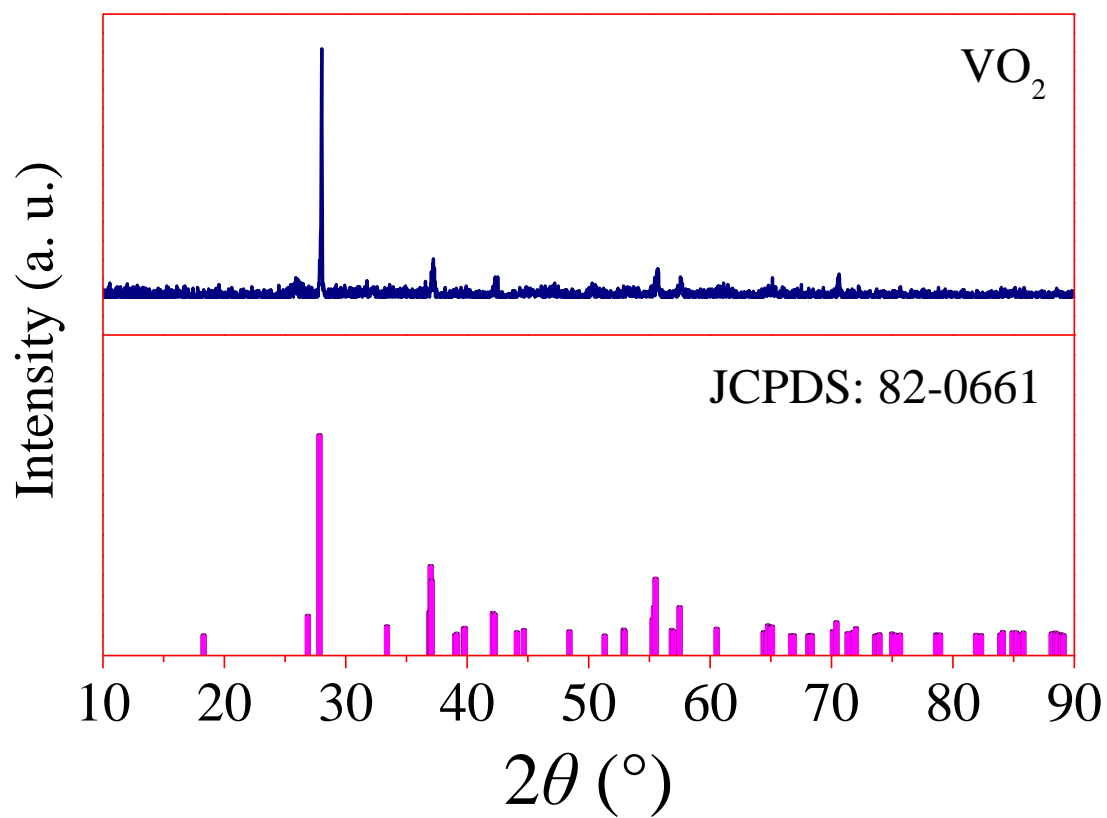


Figure S14. Characterization of VO₂, related to Figure 5.

XRD data of as-prepared VO₂.

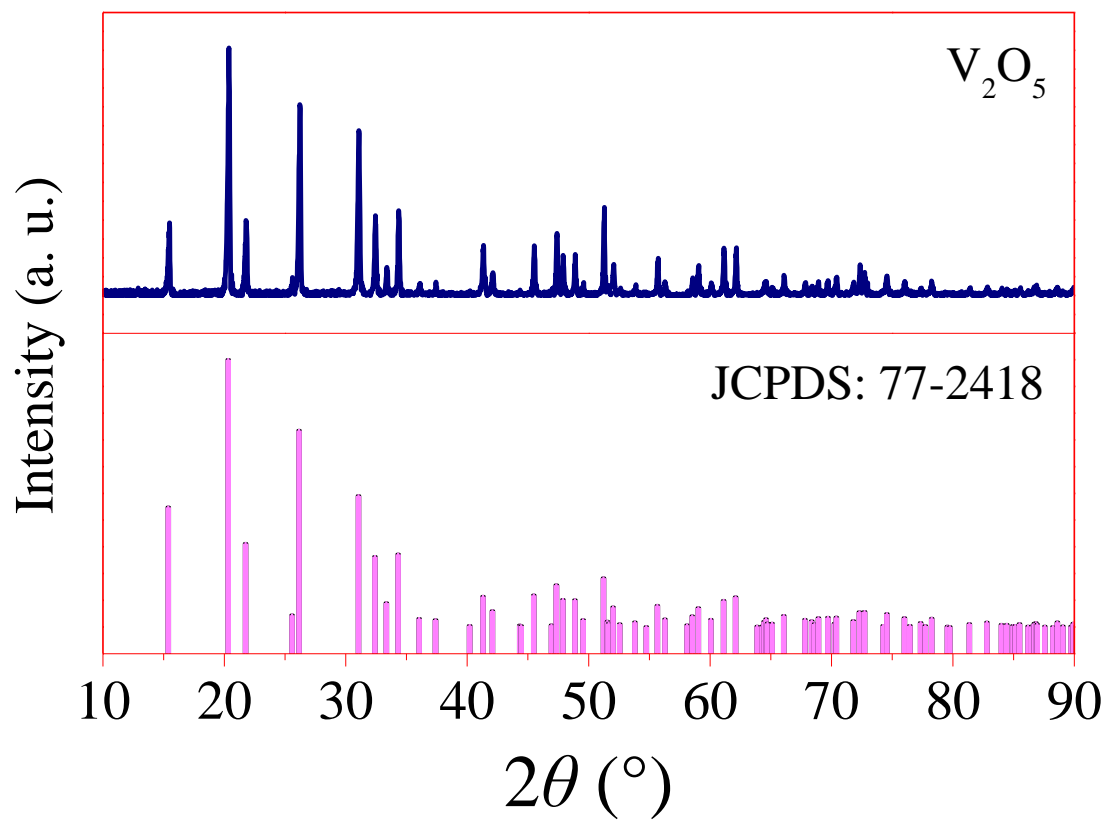


Figure S15. Characterization of V_2O_5 , related to Figure 5.

XRD data of as-prepared V_2O_5 .

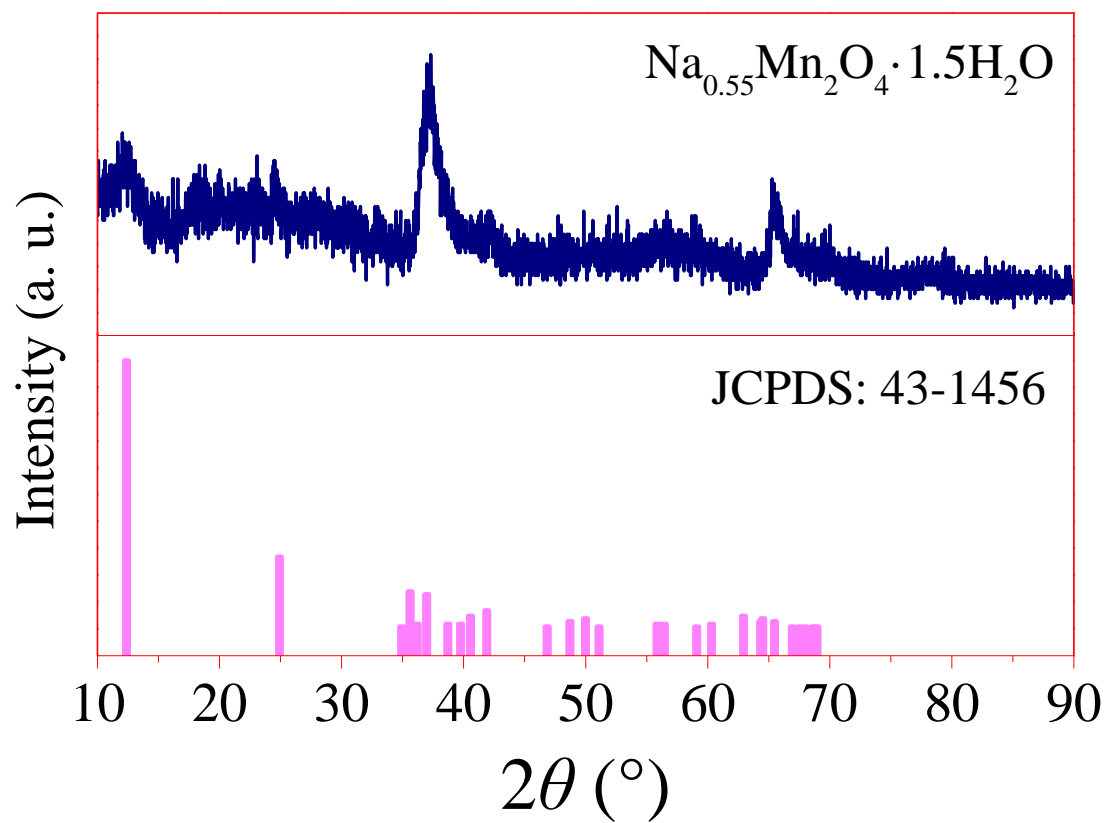


Figure S16. Characterization of $\text{Na}_{0.55}\text{Mn}_2\text{O}_4 \cdot 1.5\text{H}_2\text{O}$, related to Figure 5.

XRD data of as-prepared $\text{Na}_{0.55}\text{Mn}_2\text{O}_4 \cdot 1.5\text{H}_2\text{O}$.

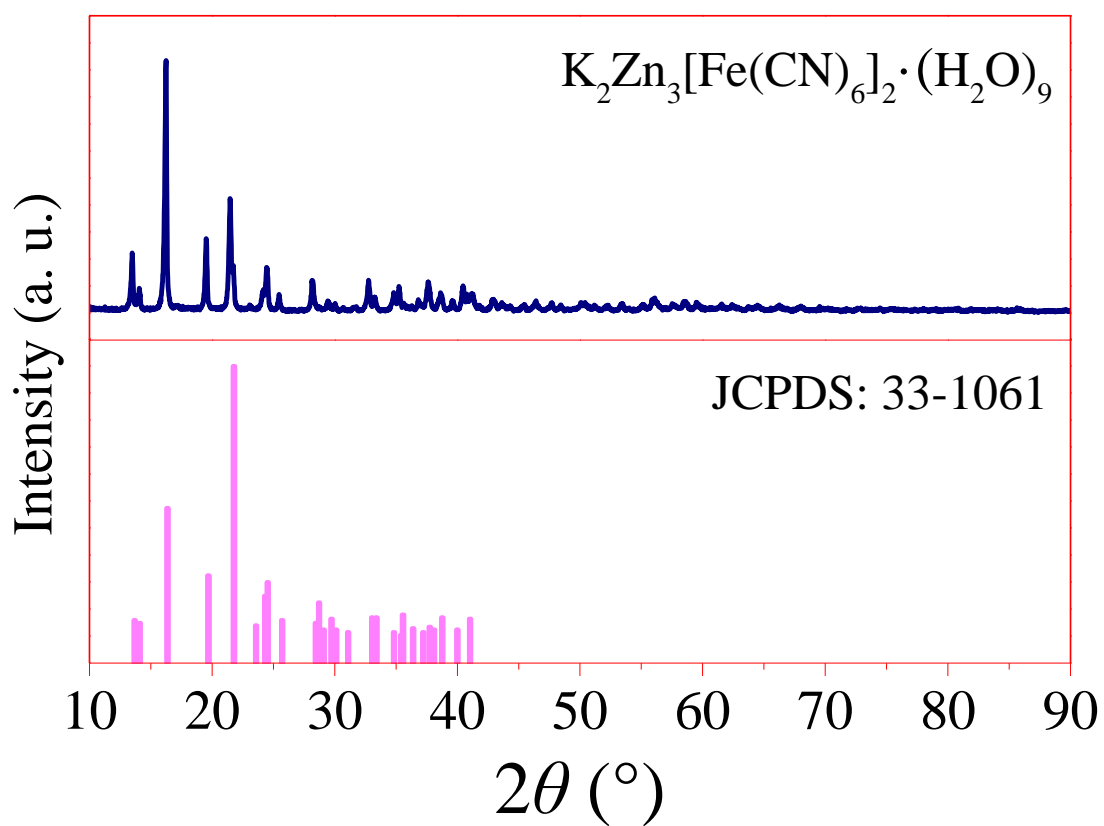


Figure S17. Characterization of $\text{K}_2\text{Zn}_3[\text{Fe}(\text{CN})_6]_2 \cdot (\text{H}_2\text{O})_9$, related to Figure 5.

XRD data of as-prepared $\text{K}_2\text{Zn}_3[\text{Fe}(\text{CN})_6]_2 \cdot (\text{H}_2\text{O})_9$.

Table S1. Electrochemical performance of Zn-based energy storage systems in ZnSO₄ aqueous electrolytes (containing dissolved oxygen), related to **Figure 3** and **Figure 5**.

Cathode material	Average discharge voltage (vs. Zn/Zn ²⁺)	Specific capacity	Rate performance	Cycle performance	Ref.
α -MnO ₂	1.44 V at 61.6 mA g ⁻¹	255 mAh g ⁻¹ at 61.6 mA g ⁻¹	31.4% retained at 308 mA g ⁻¹	50% retained after 15 cycles at 102.7 mA g ⁻¹	(Pan et al., 2016)
α -MnO ₂	1.44 V at 61.6 mA g ⁻¹	255 mAh g ⁻¹ at 61.6 mA g ⁻¹	31.4% retained at 308 mA g ⁻¹	17.6% retained after 400 cycles at 61.6 mA g ⁻¹	(Pan et al., 2016)
α -MnO ₂	1.26 V at 83 mA g ⁻¹	353 mAh g ⁻¹ at 16 mA g ⁻¹	12.2% retained at 1333 mA g ⁻¹	63% retained after 50 cycles at 83 mA g ⁻¹	(Alfaruqi et al., 2015)
α -MnO ₂	1.26 V at 10.5 mA g ⁻¹	205 mAh g ⁻¹ at 105. mA g ⁻¹	57.7% retained at 210 mA g ⁻¹	66% retained after 30 cycles at 10.5 mA g ⁻¹	(Lee et al., 2014)
α -MnO ₂	1.3 V at 10.5 mA g ⁻¹	195 mAh g ⁻¹ at 10.5 mA g ⁻¹	85.6% retained at 42 mA g ⁻¹	70% retained after 30 cycles at 42 mA g ⁻¹	(Boeun et al., 2015)
α -MnO ₂	1.3 V at 16	323 mAh	14.6% retained	46% retained after	(Alfaruqi

	mA g ⁻¹	g ⁻¹ at 16 mA g ⁻¹	at 1666 mA g ⁻¹	75 cycles at 83 mA g ⁻¹	et al., 2016)
γ -MnO ₂	1.32 V at 0.05 mA cm ⁻²	285 mAh g ⁻¹ at 0.05 mA cm ⁻²	57.8% retained at 0.5 mA cm ⁻²	63% retained after 40 cycles at 0.5 mA cm ⁻²	(Alfaruqi et al., 2015)
Layered MnO ₂	1.3 V at 50 mA g ⁻¹	289 mAh g ⁻¹ at 50 mA g ⁻¹	21.1% retained at 1000 mA g ⁻¹	35% retained after 50 cycles at 100 mA g ⁻¹	(Alfaruqi et al., 2018)
δ - MnO ₂	1.28 V at 83 mA g ⁻¹	250 mAh g ⁻¹ at 83 mA g ⁻¹	24.6% retained at 1333 mA g ⁻¹	46% retained after 100 cycles at 83 mA g ⁻¹	(Alfaruqi et al., 2015)
δ - MnO ₂	0.75 V at 12.3 mA g ⁻¹	120 mAh g ⁻¹ at 12.3 mA g ⁻¹	27.3% retained at 308 mA g ⁻¹	48% retained after 125 cycles at 12.3 mA g ⁻¹	(Han et al., 2017)
LiV ₃ O ₈	0.81 V at 16 mA g ⁻¹	256 mAh g ⁻¹ at 16 mA g ⁻¹	11.3% retained at 1666 mA g ⁻¹	75% retained after 65 cycles at 133 mA g ⁻¹	(Alfaruqi et al., 2017)
Zn ₃ V ₂ O ₇ (OH) ₂ ·2H ₂ O	0.72 V at 50 mA g ⁻¹	213 mAh g ⁻¹ at 50 mA g ⁻¹	25.4% retained at 3000 mA g ⁻¹	68% retained after 300 cycles at 200 mA g ⁻¹	(Xia et al., 2017)
V _{1-x} Al _x O _{1.52} (OH) _{0.77}	0.65 V at 15 mA g ⁻¹	156 mAh g ⁻¹ at 15	41.0% retained at 1000 mA g ⁻¹	68% retained after 50 cycles at 15 mA	(Jo et al., 2017)

		mA g ⁻¹		g ⁻¹	
V ₃ O ₇ ·H ₂ O	0.72 V at 375 mA g ⁻¹	375 mAh g ⁻¹ at 1 C	–	80 % retained after 200 cycles	(Kundu et al., 2018)
α-MnO ₂	1.44 V at 100 mA g ⁻¹	202 mAh g ⁻¹ at 0.1 A g ⁻¹	–	38% retained after 100 cycles at 0.1 A g ⁻¹	This work
Na _{0.55} Mn ₂ O ₄ ·1.5H ₂ O	1.39 V at 100 mA g ⁻¹	107 mAh g ⁻¹ at 0.1 A g ⁻¹	–	32% retained after 100 cycles at 0.1 A g ⁻¹	
VO ₂	0.68 V at 100 mA g ⁻¹	310 mAh g ⁻¹ at 0.1 A g ⁻¹	–	36% retained after 100 cycles at 0.1 A g ⁻¹	
V ₂ O ₅	0.82 V at 100 mA g ⁻¹	191 mAh g ⁻¹ at 0.1 A g ⁻¹	–	37% retained after 100 cycles at 0.1 A g ⁻¹	
K ₂ Zn ₃ [Fe(CN) ₆] ₂ ·(H ₂ O) ₉	1.03 V at 100 mA g ⁻¹	65 mAh g ⁻¹ at 0.1 A g ⁻¹	–	43% retained after 100 cycles at 0.1 A g ⁻¹	

Table S2. The peak force and the reduced modulus of Zn plate in the presence of O₂, related to **Figure 2**.

Interfacial layer	Peak force (nN)	Reduce Modulus
Zn oxides/hydroxides (Point B)	2.8	~10 GPa
Zn (Point A)	13.7	~600 MPa

Supplementary References

Alfaruqi, M. H., Gim, J., Kim, S., Song, J., Jo, J., Kim, S., Mathew, V., and Kim, J. (2015) Enhanced reversible divalent zinc storage in a structurally stable α -MnO₂ nanorod electrode. *J. Power Sources* 288, 320-327.

Alfaruqi, M. H., Gim, J., Kim, S., Song, J., Pham, D. T., Jo, J., Xiu, Z., Mathew, V., and Kim, J. (2015) A layered δ -MnO₂ nanoflake cathode with high zinc-storage capacities for eco-friendly battery applications. *Electrochem. Commun.* 60, 121-125.

Alfaruqi, M. H., Islam, S., Gim, J., Song, J., Kim, S., Pham, D. T., Jo, J., Xiu, Z., Mathew, V., and Kim, J. (2016) A high surface area tunnel-type α -MnO₂ nanorod cathode by a simple solvent-free synthesis for rechargeable aqueous zinc-ion batteries. *Chem. Phys. Lett.* 650, 64-68.

Alfaruqi, M. H., Islam, S., Putro, D. Y., Mathew, V., Kim, S., Jo, J., Kim, S., Sun, Y. K., Kim, K., and Kim, J. (2018) Structural transformation and electrochemical study of layered MnO₂ in rechargeable aqueous zinc-ion battery. *Electrochim. Acta* 276, S0013468618308995.

Alfaruqi, M. H., Mathew, V., Gim, J., Kim, S., Song, J., Baboo, J. P., Choi, S. H., and Kim, J. (2015) Electrochemically Induced Structural Transformation in a γ -MnO₂ Cathode of a High Capacity Zinc-Ion Battery System. *Chem. Mater.* 27, 3609-3620.

Alfaruqi, M. H., Mathew, V., Song, J., Kim, S., Islam, S., Pham, D. T., Jo, J., Kim, S., Baboo, J. P., and Xiu, Z. (2017) Electrochemical Zinc Intercalation in Lithium Vanadium Oxide: A High-Capacity Zinc-Ion Battery Cathode. *Chem. Mater.* 29, 1684-1694.

Boeun, L., Hae, Ri L., Haesik, K., Kyung, Yoon C., Byung, Won. C., and Hyung, O. S. (2015) Elucidating the intercalation mechanism of zinc ions into α -MnO₂ for

rechargeable zinc batteries. *Chem. Commun.* *51*, 9265-9268.

Ding, J. W., Du, Z. G., Gu, L. Q., Li, B., Wang, L. Z., Wang, S. W., Gong, Y. J., and Yang, S. B. (2018) Ultrafast Zn²⁺ Intercalation and Deintercalation in Vanadium Dioxide. *Adv. Mater.* *30*, 6.

Han, S. D., Kim, S., Li, D., Petkov, V., Yoo, H. D., Phillips, P. J., Wang, H., Kim, J. J., More, K. L., and Key, B. (2017) Mechanism of Zn Insertion into Nanostructured δ -MnO₂: A Nonaqueous Rechargeable Zn Metal Battery. *Chem. Mater.* *29*, 4874-4884.

Hu, Z. M., Xiao, X., Jin, H. Y., Li, T. Q., Chen, M., Liang, Z., Guo, Z. F., Li, J., Wan, J., Huang, L., Zhang, Y. R., Feng, G., and Zhou, J. (2017) Rapid mass production of two-dimensional metal oxides and hydroxides via the molten salts method. *Nat. Commun.* *8*, 9.

Jo, J. H., Sun, Y-K., and Myung, S-T. (2017) Hollandite-type Al-doped VO_{1.52}(OH)_{0.77} as a zinc ion insertion host material. *J. Mater. Chem. A* *5*, 8367-8375.

D. Kundu, S. H. Vajargah, L. Wan, B. Adams, D. Prendergast and L. F. Nazar, (2018) Aqueous vs. nonaqueous Zn-ion batteries: consequences of the desolvation penalty at the interface. *Energy Environ. Sci.* *11*, 881-892.

Lee, B., Yoon, C. S., Lee, H. R., Chung, K. Y., Cho, B. W., and Oh, S. H. (2014) Electrochemically-induced reversible transition from the tunneled to layered polymorphs of manganese dioxide. *Sci. Rep.* *4*, 6066.

Pan, H., Shao, Y., Yan, P., Cheng, Y., Han, K. S., Nie, Z., Wang, C., Yang, J., Li, X., and Bhattacharya, P. (2016) Reversible aqueous zinc/manganese oxide energy storage from conversion reactions. *Nat. Energy* *1*, 16039.

Shen, X., Li, Y., Qian, T., Liu, J., Zhou, J., Yan, C., and Goodenough, J. B. (2019) Lithium anode stable in air for low-cost fabrication of a dendrite-free lithium battery. *Nat. Commun.* *10*, 900.

Xia, C., Guo, J., Lei, Y., Liang, H., Zhao, C., and Alshareef, H. N. (2017) Rechargeable Aqueous Zinc-Ion Battery Based on Porous Framework Zinc Pyrovanadate Intercalation Cathode. *Adv. Mater.* *30*, 1705580.

Zhang, L., Chen, L., Zhou, X., and Liu, Z. (2015) Towards High-Voltage Aqueous Metal-Ion Batteries Beyond 1.5 V: The Zinc/Zinc Hexacyanoferrate System. *Adv.*

Energy Mater. 5, 1400930.

Zhang, N., Dong, Y., Jia, M., Bian, X., Wang, Y. Y., Qiu, M. D., Xu, J. Z., Liu, Y. C., Jiao, L. F., and Cheng, F. Y. (2018) Rechargeable Aqueous Zn-V₂O₅ Battery with High Energy Density and Long Cycle Life. ACS Energy Lett. 3, 1366-1372.